



DEGREE PROJECT IN MATERIALS SCIENCE AND ENGINEERING,
SECOND CYCLE, 30 CREDITS
STOCKHOLM, SWEDEN 2020

Development of corrosion resistant coatings using natural biopolymer and pollen

ALESSANDRO ARMANI

ABSTRACT

Corrosion is a mechanism that highly reduces the lifetime of metals in different environments, especially in water or moisture environment. The worldwide maintenance cost due to corrosion is estimated in billions of dollars per year, and actual solutions in terms of coating usually contains toxic or environmentally harmful species. With an always increasing restriction by environmental restraints and regulations, a sustainable solution is urgently needed.

Chitosan, easily obtained from chitin, the second most abundant biopolymer on earth, can be the solution to many problems. Crustacean shell waste is one of the major sources of chitin. Its resource efficiency, biocompatibility, and versatile physicochemical properties for chelation and crosslinking make chitosan a promising candidate as matrix material for biobased anticorrosive application.

The purpose of the Master Thesis is to combine the properties of chitosan with the high porosity of bee pollen as anticorrosive agent carrier to obtain a fully sustainable solution for anticorrosive protection. The objective of this very ambitious project is to produce a composite material with a triple action: anticorrosive protection of metal surfaces, self-healing property of the coating and anti-biofouling activity.

Results show that a biopolymer composite in forms of suspension or coatings with all desired components could be achieve. Specifically, a biopolymer nanocomposite composed of chitosan matrix, embedded with pollen grains that were loaded with anticorrosion agent 2-mercatobenzothiazole (MBT) in advance, and with zinc oxide nanoparticles have been produced.

The physicochemical characterization of the biopolymer composite and its coatings, as well as electrochemical impedance spectroscopy (EIS) measurements on stainless steel plate with such coatings, suggest that a uniform and compact coating is obtained. Despite its good hydrophobicity with maximum contact angle $134.32 \pm 3.84^\circ$ with top coating, the chitosan nanocomposite coating is still permeable to water, partially because of the relatively big size of pollen (ca. 20 μm) that introduces gaps and interferes integrity of the coating. Therefore, a full immersion corrosion resistance is not achieved. In conclusion, phase transfer of hydrophobic pollen into hydrophilic chitosan matrix, MBT loading in pollen, ZnO encapsulation in chitosan, as well as crosslinking of chitosan, were successfully carried out. A coating based on such biopolymer nanocomposite is prepared on stainless steel and investigated on its anti-corrosion property. Future work will be choosing a proper sized pollen as a microcontainer to enhance the integrity of the coating, and eventually endow the coating with the three-in-one function, i.e., anticorrosion, antimicrobial, and self-healing.

SAMMANFATTNING

Korrosion är en mekanism som kraftigt reducerar livslängden för metaller i olika miljöer, särskilt i vatten- eller fuktmiljö. De globala underhållskostnaderna på grund av korrosion uppskattas i miljarder dollar per år, och faktiska lösningar med avseende på beläggning innehåller vanligtvis giftiga eller miljöfarliga arter. Med en ständigt ökande begränsning genom miljörestriktioner och bestämmelser krävs det en hållbar lösning.

Kitosan, den näst vanligaste biopolymeren, kan vara lösningen på många problem. Skaldjuravfall är en av de viktigaste källorna till kitosan. Dess resurseffektivitet, biokompatibilitet och mångsidiga fysikalisk-kemiska egenskaper för kelering och tvärbinding gör kitosan till en lovande kandidat som matrismaterial för biobaserade antikorrosiva applikationer.

Syftet med denna masteruppsats är att kombinera egenskaperna hos kitosan med den höga porositeten hos bipollen som antikorrosivt medel för att erhålla en helt hållbar lösning för korrosionsskydd. Målet med detta mycket ambitiösa projekt är att producera ett sammansatt material med en tredubbel verkan: korrosionsskydd för metallytor, självhelande egenskap hos beläggningen och anti-biobeväxningsaktivitet.

Resultaten visar att en biopolymerkomposit i form av suspension eller beläggningar med alla önskade komponenter kan uppnås. Specifikt har en biopolymer-nanokomposit sammansatt av kitosanmatris med inbäddade pollen, som i förväg packats med antikorrosionsmedlet 2-mercaptobenzotiazol (MBT) och med zinkoxid-nanopartiklar, producerats.

Den fysikalisk-kemiska karakteriseringen av biopolymerkompositen och dess beläggningar, liksom elektrokemiska impedansspektroskopimätningar (EIS) på rostfri stålplåt med sådana beläggningar tyder på att en enhetlig och kompakt beläggning erhålls. Trots sin goda hydrofobi med maximal kontaktvinkel $134,32 \pm 3,84^\circ$ med toppbeläggningen, är nanokompositbeläggningen av kitosan fortfarande permeabel för vatten, delvis på grund av den relativt stora storleken hos pollen (ca. 20 μm) som introducerar luckor och stör integriteten hos beläggningen. Därför uppnås inte en fullständig immersionskorrosionsbeständighet. Sammanfattningsvis genomfördes fasövergång av hydrofob pollen till hydrofil kitosanmatris, MBT-packning i pollen, ZnO-inkapsling i kitosan, samt tvärbinding av kitosan med framgång. En beläggning baserad på sådan biopolymer-nanokomposit framställs på rostfritt stål och undersöks med avseende på dess korrosionsegenskaper. Framtida arbete kommer att bestå i att välja en lämplig storlek av pollen som en mikrobehållare för att förbättra beläggningens integritet, och så småningom förse beläggningen med tre-i-ett-funktionen, dvs. antikorrosion, antimikrobiell och självhelande.

FIGURE INDEX

- Figure 1: Main forms of corrosion
- Figure 2: Schematic representation of corrosion electrochemical process
- Figure 3: Ideal coating equivalent circuit
- Figure 4: Quasi-ideal coating equivalent circuit
- Figure 5: Nyquist (a) and Bode (b-c) plots of quasi-ideal coating
- Figure 6: Nyquist plot example with representation of $|Z|$ and phase angle
- Figure 7: Failed coating equivalent circuit
- Figure 8: Deacetylation process
- Figure 9: Pollen grain SEM image
- Figure 10: Chemical structure of MBT
- Figure 11: Release profile of MBT from CS-MBT in different conditions
- Figure 12: Schematic mechanism of photocatalysis of ZnO
- Figure 13: Schematic representation of pollen, OA and PMAO system
- Figure 14: Schematic representation of EDC/NHS crosslinking
- Figure 15: Schematic illustration of chitosan-glutaraldehyde crosslinking mechanism
- Figure 16: SEM schematic representation
- Figure 17: Schematic representation of FT-IR, ATR mode
- Figure 18: First derivative curves for different N-acetyl-D-glucosamine concentrations
- Figure 19: Peak heights at 199 nm for different N-acetyl-D-glucosamine concentrations, fit plot and linear regression
- Figure 20: UV-Vis curves for different amount of MBT in ethanol
- Figure 21: Peak heights at 320 nm for different MBT concentrations, fit plot and linear regression
- Figure 22: UV-Vis profile of pollen/CS/ZnO polymer, 10 (blue) and 100 (red) times dilution
- Figure 23: SEM images of treated pollen, with only ethanol (a) and with formaldehyde (b)
- Figure 24: Optical microscope images from lower to higher magnification (a-d)
- Figure 25: optical microscope images to focus on microcracks (a) and hall defects (b) in failed coating
- Figure 26: SEM images of coating, low magnification (a) and a detail (b)
- Figure 27: SEM images of tannic acid primer sample (a) and MUA primer sample (b)
- Figure 28: SEM image of MUA primer and chitosan sample
- Figure 29: SEM images of fine (a) and coarse (b) grinded surface followed by MUA primer, chitosan layer and coating
- Figure 30: SEM images of MUA primer, chitosan first layer and polymer
- Figure 31: Optical microscope image of MUA primer, chitosan layer and polymer
- Figure 32: FT-IR curves of non-crosslinked chitosan, crosslinked chitosan and coating
- Figure 33: Contact angle image of non-top coated sample (a), PMAO top coated sample (b) and stearic acid top coated sample (c)
- Figure 34: EIS plot of PMAO top coated sample. Nyquist plot (a) and Bode plot, phase vs. frequency (b)
- Figure 35: Equivalent circuit for PMAO top coated sample
- Figure 36: EIS plot of different coated samples. Nyquist plot (a) and Bode plot, phase vs. frequency (b)
- Figure 37: Equivalent circuits for different coatings

LIST OF ACRONYMS AND ABBREVIATIONS

ATR	Attenuated total reflectance
CS	Chitosan
DCM	Dichloromethane
DDA	Degree of deacetylation
EDC	1-(3-Dimethylaminopropyl)-3-ethylcarbodiimide Hydrochloride
EIS	Electrochemical impedance spectroscopy
FT-IR	Fourier transform infrared spectroscopy
GA	Glutaraldehyde
MBT	2-Mercaptobenzothiazole
MUA	11-mercaptoundecanoic acid
NaOH	Sodium hydroxide
NHS	<i>N</i> -hydroxysuccimide
OA	Oleic acid
OCP	Open circuit potential
OM	Optical microscope
PEMA	Poly(ethylene-alt-maleic anhydride)
PMAO	Poly(maleic anhydride-alt-1-octadecene)
SA	Stearic acid
SAM	Self-assembled monolayer
SEM	Scanning electron microscope
SS	Stainless Steel
TBT	Tributyltin
THF	Tetrahydrofuran
VOCs	Volatile organic compounds
ZnO NPs	Zinc oxide nanoparticles

TABLE OF CONTENTS

1	INTRODUCTION	1
1.1	The corrosion problem	1
1.2	Corrosion	1
1.2.1	Classification of corrosion	1
1.2.2	Corrosion principles	2
1.2.3	Corrosion in water	5
1.2.4	Anticorrosion techniques	5
1.2.5	Environment and materials	8
1.2.6	Corrosion principles and characterization of anti-corrosion organic barrier coating	9
1.3	Chitosan	12
1.4	Pollen	14
1.5	2-Mercatobenzothiazole	15
1.6	Biofouling	16
1.7	Zinc oxide nanoparticles	18
1.8	Objective of the thesis	19
2	EXPERIMENTAL	20
2.1	Materials	20
2.2	Methods	20
2.2.1	Deacetylation of chitin	20
2.2.2	Pollen	21
2.2.3	Phase transfer and cross-linking	21
2.2.4	Surface preparation	24
2.2.5	Coating methods and surface coating	24
2.3	Characterization	26
2.3.1	Material characterization	26
2.3.2	Characterization of coating	27
2.3.4	Evaluation of properties	28
3	RESULTS AND DICUSSION	30
3.1	Degree of deacetylation	30
3.2	2-Mercaptobenzothiazole content	31
3.3	Pollen	34
3.4	Viscosity	34
3.5	Sample morphology	35
3.5.1	Optical microscope	35

3.5.2 SEM	36
3.6 Sample performances	37
3.6.1 Thickness	37
3.6.2 Surface attachment	37
3.6.3 FT-IR.....	40
3.6.4 Water contact angle.....	41
3.6.5 Anticorrosion behavior	42
4 CONCLUSIONS.....	46
5 FUTURE WORK.....	48
6 ACKNOWLEDGMENTS	49
7 REFERENCES.....	50

1 INTRODUCTION

1.1 The corrosion problem

Corrosion can be defined as a destructive attack on a material caused by its interaction with the environment [1]. The American Society for Testing and Materials defines corrosion as “the chemical or electrochemical reaction between a material, usually a metal, and its environment that produces a deterioration of the material and its properties” [2]. Corrosion represents one of the biggest issues when dealing with metals and non-metals material in harsh environment and non. There are several examples of catastrophic corrosion damage in recent history, such as the oil spills that a 540 m³ oil discharge happened in Santa Barbara during 2015, or the explosion of a gas pipeline in New Mexico during 2000 [3].

Apart from the visible environmental pollution or human losses in such catastrophes that were the result of severe corrosion problems, economic cost of corrosion is enormous. Over the last fifty years, a large number of studies on corrosion cost have been conducted. Based on different approaches and using different tools, all the studies converge on the idea that the cost of corrosion represents an average of 3-4% of the gross domestic product (GDP)[4]. Following this estimation, the annual global corrosion cost would be between US\$ 375 billion and US\$ 875 billion [4]. A 2005 paper [5] evaluated the direct corrosion cost for USA, not including infrastructure, utilities and transportation, that would be around US\$ 276 billion, while including the indirect cost would arrive up to US\$ 551.4. Despite corrosion is an inevitable phenomenon, several methods to prevent or delay the corrosion are described in section 1.2.4. All these methods have the aim of prolonging the lifetime of metal and non-metal materials subjected to corrosion, that will save the corrosion cost.

1.2 Corrosion

1.2.1 Classification of corrosion

Corrosion represents a widespread phenomenon and a problem that almost all the materials are affected by and over centuries many classifications have been attributed to corrosion. Some prefers dividing corrosion in low-temperature and high-temperature corrosion, others prefer direct combination (or oxidation) and electro-chemical corrosion, while most of the people prefer dividing corrosion in dry and wet corrosion [6]. Wet corrosion is referred to a situation when a liquid is involved, mostly aqueous solution or electrolytes. Dry corrosion, on the contrary, is referred to a situation when a liquid phase is not present, and gases and vapours are usually the corrodents [6].

As well as dividing corrosion into wet and dry, corrosion can also be divided based on mechanism and media [7]. The division of corrosion types by mechanism individuates eight main types: uniform, galvanic, crevice, pitting, intergranular, selective leaching, erosion and stress corrosion [6]. A schematic representation of different types of corrosion and their effect is shown in Figure 1Figure 1: Main forms of corrosion [8].

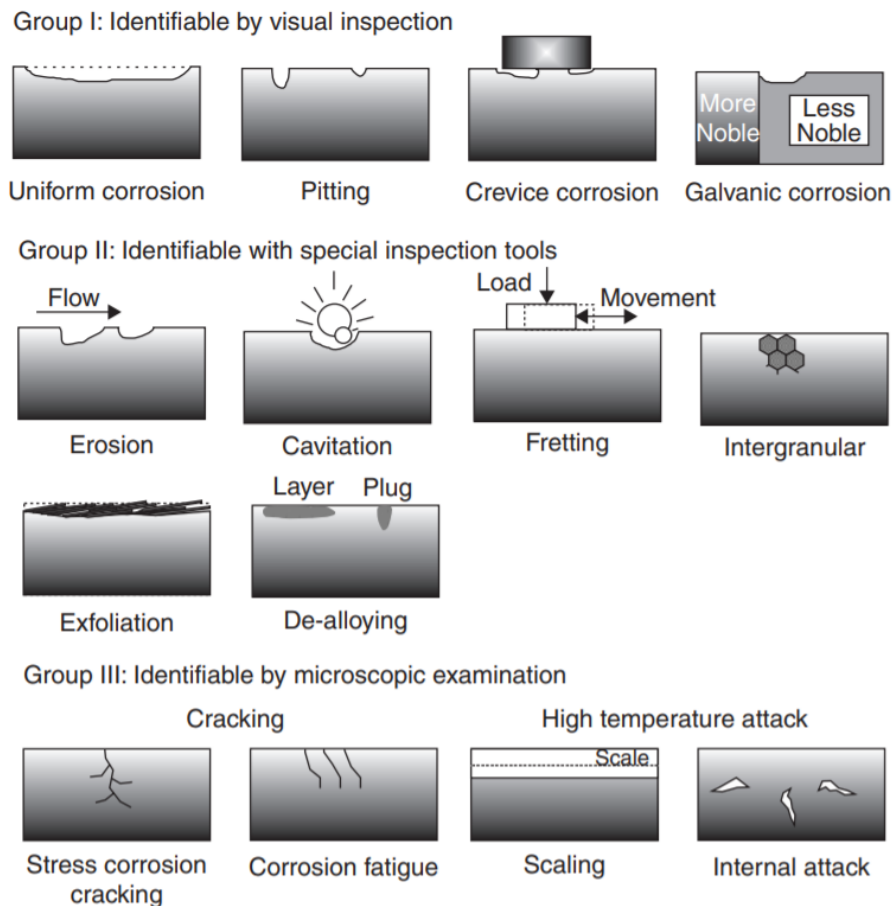


Figure 1: Main forms of corrosion [8]

Different types of corrosions based on media include atmospheric corrosion, natural and seawater corrosion, corrosion in soils, reinforced concrete and microbes and biofouling corrosion. [1, 7].

1.2.2 Corrosion principles

1.2.2.1 Electrochemical reactions

Corrosion, in a simplistic way, can be seen as the mere effect of a redox reaction. Despite we are used to imagine a redox reaction occurring in an electrochemical cell with distinct electrodes, in metal corrosion the metal plate acts as anode as well as cathode. Here, steel will be considered as example in redox reaction occurring during corrosion (Figure 2).

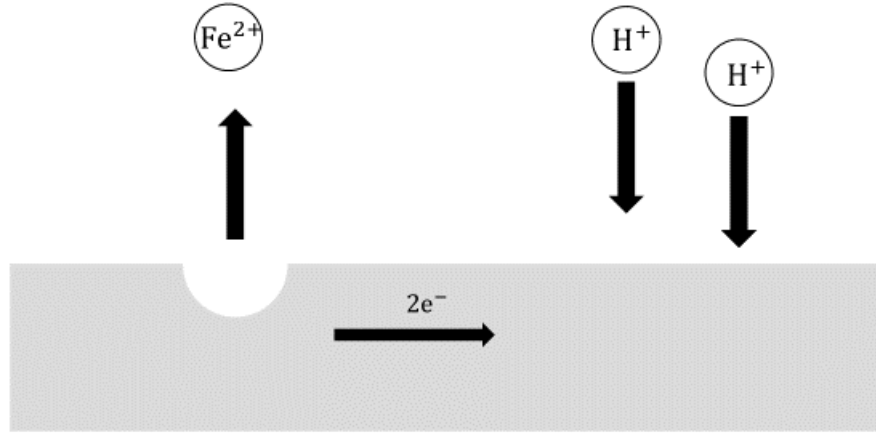
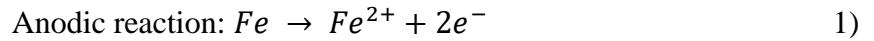
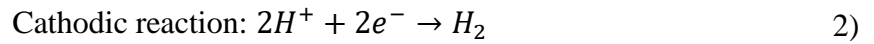


Figure 2: Schematic representation of corrosion electrochemical process

Iron is transformed in iron ions according to Eq. 1



The reaction produces electrons that flow through the metal to another site where hydrogen ions are reduced to hydrogen (Eq.2).



The two reactions must occur at the same times and with equivalent rates [8]. The number of electrons generated by anodic reaction depends on the metal involved in the corrosion process. Thanks to Faraday's law, we can correlate the mass loss directly to the current and the number of electrons (Eq.3)

$$Q = F \cdot \Delta N \cdot n \quad 3)$$

Where F is Faraday's constant, ΔN is the mass loss in moles and n is the number of generated electrons. Q can be expressed in terms of current as:

$$Q = \int_0^t I \cdot dt \quad 4)$$

Despite hydrogen production is the most common cathodic reaction that occurs during corrosion phenomenon, many other reactions can occur. An example, when in atmospheric environment or in solution is contact with atmosphere, is the oxygen reduction (Eq. 5)



Other cathodic reactions can be metal reduction, less common but that leads to very dangerous corrosion problems.

During a corrosion phenomenon, more than one oxidation and reduction reaction can occur. In this case, the number of electrons flowing in the metal would increase, increasing the corrosion rate.

Another important factor that needs to be considered is the surface area. Despite the anodic and cathodic reactions have the same rate and currents, this does not mean that they have the same current density. When the difference between cathodic and anodic surface is very large, such corrosion mechanisms as galvanic corrosion are strongly affected and corrosion results may be devastating.

1.2.2.2 Thermodynamic aspects

Nernst Equation correlates the potential of a cell, given by the difference of potentials of the two electrodes, to the concentration of participating ions and other chemicals. In a reaction



Given a Q_{reaction} as:

$$Q_{\text{reaction}} = \frac{a_M^m \cdot a_N^n \dots}{a_A^a \cdot a_B^b \dots} \quad 7)$$

Where a_X^x represents the chemical activity of a species, the overall potential of an electrochemical reaction is related to the standard potential of the reaction (E^0) by Nernst equation, that can be written as:

$$E = E^0 - \frac{RT}{nF} \ln Q_{\text{reaction}} \quad 8)$$

The corrosion of a metal is associated with a change in the Gibbs free energy, accordingly to Eq.9 [9]

$$\Delta G = -n \cdot F \cdot E_{\text{cell}}^0 \quad 9)$$

1.2.2.3 Kinetic aspects

Thermodynamics considerations can be used to predict if corrosion will take place, but it is only through kinetic that corrosion rate can be determined. Kinetic considerations are mostly based on the concept of overpotential. It is used to quantify the polarization, described as the difference between the resultant potential (E) and the potential of an individual reaction that can take place at anodic or cathodic site (E_{eq}) [8]. Three are the polarizations types: activation polarization, concentration polarization and ohmic drop. Activation polarization is used to describe the charge transfer kinetic of an electrochemical reaction, while concentration polarization describes the mass transfer kinetic of

an electrochemical reaction. Last, ohmic drop considers the electrolytic resistivity of a specific environment [8].

1.2.3 Corrosion in water

Corrosion of iron in fresh water is influenced by many factors, as hardness and chloride content, but it is mainly affected by oxygen presence. Oxygen diffusion to metal surface is a corrosion rate determining step [10]. Corrosion in natural waters is not highly dependent on the grade of iron, except for $\text{pH} < 4$ and > 10 , where hydrogen evolution and passivation, respectively, occurs [10]. Fresh waters can be classified as soft or hard; in hard water corrosion by oxygen diffusion is generally limited by carbonates. They usually deposit on metal surface creating a protection layer that inhibits oxygen diffusion [6, 10].

Seawaters have a salt content of 3.4% and a pH of 8. Seawater corrosion is mainly affected by oxygen content, velocity, temperature and biological organisms [6]. Despite the chloride concentration should result in high corrosion rate [11], corrosion in seawater is in average less than the one in fresh waters. This is mainly due to protective action by CaCO_3 and in smaller amount by $\text{Mg}(\text{OH})_2$ that creates a surface layer that inhibits oxygen diffusion [10]. Splash zones are the most corrosion sensitive regions because a water film layer forms and corrosion products are frequently washed away [10].

In water environment with normal oxygen content, the oxygen reduction reaction (ORR) can be as in Eq. 10



With Eq.1 anodic reaction and Eq.10 cathodic reaction, the ferrous ions can react with hydroxyl ions and generate ferrous hydroxide [12]. In excess of oxygen, ferrous hydroxide would be oxidized in insoluble product, while in presence of NaCl, ferrous chlorides are formed with rust as final product of a cyclic oxidation [12].

1.2.4 Anticorrosion techniques

Many techniques have been developed over centuries to protect surfaces from corrosion. Depending on material, environment and mechanism involved, different solutions can be applied to successfully delay corrosion phenomena. Four are the major mechanisms that have been developed: cathodic protection, anodic protection, corrosion inhibitor and protective coating. In this section, a brief description of the first three protective methods will be done, while attention will be focused on protective coatings, with particular regard to organic protective coatings.

Cathodic protection is based on a very simple assumption: through application of a cathodic current, anodic dissolution will be minimized. In substance, a current will be applied onto the surface to supply electrons for cathodic reaction (Eq. 2 above), thus avoiding the electrons to come from the metal surface, that will be thus preserved. Two main methods can be used to supply cathodic current: by an external power supply or by galvanic coupling [6]. Typical concern when dealing with cathodic protection is the applied current. Too low current will result in metal corrosion, too high current could lead to degradation of coating and hydrogen embrittlement [1].

Anodic protection is based on the creation of a protective film on metals through application of an anodic current [1]. It could seem that the application of anodic current would lead to an increase of the dissolution rate of a metal. Nevertheless, it does not for some metals that show active-passive transitions [6]. Anodic protection cannot thus be applied to all metals, but for those it can it shows very good protection against corrosion.

A *corrosion inhibitor* is defined as a substance then, when added in small amounts in an environment, decrease the rate of corrosion [1]. There are several types of classifications of inhibitors: per mechanism, including increasing anodic or cathodic polarization behaviour, reducing the movement or diffusion of ions to metallic surface, and increasing the electrical resistance of the metallic surface. Most of the authors prefer dividing inhibitors by their chemical functionality: inorganic inhibitors, organic anionic and organic cationic inhibitors [1].

Protective coatings represent the most common corrosion protection method [1]. Coatings do not have any role in structural strength, as their function is to ensure the protection of the metal and its mechanical properties preservation over time. Coating must be continuous and not show any damage, as only a small failure in coating integrity would lead to focalized and dangerous corrosion phenomenon. Coating act following one of these three mechanisms: barrier effect, cathodic protection or inhibition/passivation [10]. The first mechanism is a physical barrier that isolate the metal from the environment. In cathodic protection the applied coating act as sacrificial anode. These three mechanisms can act together or separately.

Corrosion protective coatings are usually divided into three main groups: metallic coatings, inorganic coatings, and organic coatings. In this section a brief description of the first two groups will be given while attention will be focused on organic coatings, as they represent the case study.

Metallic coating is obtained through application of a metal layer over a core metal, providing new properties to the core metal [1]. The corrosion resistance performances are ensured by the applied metal, while core metal will provide mechanical strength. Metallic coatings can be divided into two groups, cathodic and anodic [10]. Cathodic metallic coating involves the use of a surface metal that is more noble than the core metal, while in anodic metallic coating the mechanism is the opposite. In cathodic coating, the applied metal mostly acts as mere physical barrier, even if in some cases the substrate metal can also be anodically protected. Together with physical barrier, anodic metallic coating would provide cathodic protection for some uncoated areas [10]. The most common metals used for metal coating are cadmium, nickel, zinc, aluminum, and chromium. Various are also the techniques used to apply metal coating: flame spraying, electrodeposition, cladding and hot dipping are some examples [6].

Inorganic coatings involve the use of treatments that modify the surface layer of metals to metal oxide or compound that shows better corrosion properties than the bulk metal [1] and can be obtained through chemical action. The main inorganic coatings techniques are anodizing, chromate filming, phosphate coating, nitriding, and passive films. These methods have the aim to provide surface layers for corrosion protection, both by improving the properties of naturally originated oxide films (as thickness or homogeneity) or by creating surface layers with addition of external compounds.

1.2.4.1 Organic coatings

In average, organic coatings contain 15 to 20 components, that can be modified based in the major outcomes required [1]. Organic coatings are modelled on design needs, based on the desired protection method. Organic coating, in fact, can act enhancing *impermeability*, thus isolating the metal from the environment, they can enhance *inhibition* by reacting with the environment and creating protective layers, and they can improve *cathodic protection* through proper pigments [1].

Pigments are only one of the main components of an organic coating. Others are binder, solvent, extenders, and other additives (driers, thickeners, etc.).

Binders ensure coherence and uniformity to the coating [1]. They are generally divided based on chemical reactions in oxygen-reactive binder (such as alkyds and epoxy esters), lacquers (as polyvinyl chloride polymers and chlorinated rubbers), heat-conversion binders (hot melts and powder coating as examples), coreactive binders (epoxies and polyurethanes), condensation binders, coalescent binders and inorganic binders.

Pigments are dry powder with various nature, from minerals to organic compounds, with multiple purposes. Some examples include protection of resin binder, corrosion inhibition and/or resistance, improvements of adhesion and modification of color [1]. Zinc phosphates are probably the most common pigments in anticorrosion coatings [1].

Multiple solvents are usually used for a single coating [1]. Different types of solvents give different properties as viscosity, drying speed and spray ability. Different categories of solvents include aliphatic and aromatic hydrocarbons, ketones, esters alcohols and esters. Last, water is becoming always more important as solvent since the environmental regulations to reduce volatile organic compounds (VOCs).

Structurally, three main parts can be identified in organic coatings: primer layer, intermediate layer and top coat [10]. Primers usually contain pigments that enhance inhibition or cathodic protection of the base metal and they ensure attachment to metal support, while top coats usually contain color pigments and extenders to improve the barrier effect [10]. Intermediate layer ensure the thickness of the coating, and must be strongly bonded to both primer and topcoat [1]. Moreover, ideally it is chemically resistant, it increases the electrical resistance of the coating and it is resistant to moisture transfer [1].

Three are the main procedures to be considered when dealing with organic coatings: (i) surface preparation, (ii) selection of primer and (iii) selection of top coats [6]. The failure of one of these operations will lead to the failure of coating. A poor adhesion of the coating to the surface will lead to peeling off of the coating, while if the two first factors are wrong, regardless the top coat, early failure will occur [6]. Surface preparation is usually performed to obtain a clean and rough surface, with increased mechanical bonding (teeth). Another bonding way is chemical bonding, for which the primer layer must be chosen carefully to have high chemical affinity with metal substrate. Last, topcoats must be chosen based on the environment the coating is going to work in. In water environment a hydrophobic behavior of coating surface is usually preferred. Despite the mechanism of barrier coating relies on ionic impermeability of the coatings and not on water and oxygen permeability [9], diffusion of water in the coating is to be avoided. Barrier coatings merely act as physical barrier between the substrate metal and the environment. The resistance to transport of water,

ions and oxygen is of utmost importance to prevent the metal from corrosion [10]. The ability of controlling the absorption and transport of these species will be a determining step for corrosion protection. The cathodic reaction rate is in fact determined by film resistance and its potential [13].

1.2.5 Environment and materials

Plastic-based objects are by far some of the most spread items worldwide. Microplastic is defined as any fragmented plastic material with size less than 5 mm and represents one of the newest and most concerning forms of pollution [14]. The huge consumption of plastic-based items and the negligence in dealing with its disposal led to serious pollution issues. Microplastic by-products from many industries and wastewater treatment plants [15] are reversed in sea waters and represent a huge new threat to environment. Microplastic can be divided into primary, when intentionally produced in small-size for industrial purposes, and secondary, fragmented particles from polymer products [16]. Microplastic are indigestible for many small aquatic organisms and their hydrophobic nature leads to organic toxicants accumulation up to a million times higher than in the rest of water [16].

Current solutions to deal with microplastics involve both its removal from water or its complete degradation [14]. In the first case, a physical separation is achievable by multiple means, as discfilter, rapid sand filtration, dissolved air flotation and membrane bioreactor [17]. Degradation of microplastic is preferable to separation because direct fragmentation in non-harmful molecules can be achieved, thus being a time-consuming technique. Different types of degradation can be used, as physical degradation, chemical degradation, photodegradation and biodegradation by organisms [18]. Photodegradation in particular represents a novel solution that can be successfully used also with visible light [19].

The main sources of microplastic, as mentioned before, are industries such as cosmetic and textile [20]. Nevertheless, a source of microplastic with direct dispersion in seawaters are paints used in maritime environment. Many components, mostly binders, of organic paints are plastic-based and can be easily dispersed in waters, thus increasing the microplastic concentration. Despite paints are not considered the major source of microplastic, efforts in decreasing paints' effect on maritime pollution should be done.

Environmental issues and regulations, as the aforementioned microplastic pollution and restrictions on volatile organic compounds (VOCs), are leading to a focus on bio-solutions in all the industrial fields, paints and coating comprehended. Many organic coating constituents' materials, listed at the beginning of 1.2.4.1, are not biobased materials, even if attempts in using biomaterials for anticorrosion purposes have been made. Nevertheless, many solutions involve the use of biomaterials as support of already common solutions for anticorrosive coating [21]. Since the variety of functions that the organic coating needs to ensure, as good adhesion to metal surface, isolation of substrate from environment, etc. it is difficult to obtain a fully natural anticorrosive coating. Attempts have been done using chitosan (CS) as biopolymer matrix [22, 23], with proved increase in anticorrosion performances. Although CS-based green coating have been developed for anticorrosion protection, solutions involving coating multiple action are still underdeveloped [24].

1.2.6 Corrosion principles and characterization of anti-corrosion organic barrier coating

As already mentioned, one of the protection mechanisms of organic coating is acting as a physical barrier between the protected metal and the environment. The corrosion of an organic-coated metal is due to the diffusion of water, oxygen and ions to the metal-coating interface [25]. Despite the diffusion of these species is inevitable over time, the most severe corrosion forms on coated metals are due to defects into the coating, such as cut edges or scratches [25]. The overall performances of a barrier coating are based on its resistance to species transport and its adhesion to the metal surface [12, 25].

The most common characterization technique for coating is Electrochemical impedance spectroscopy (EIS). EIS can provide information on the resistance of the coating to the diffusion of ions and water [25]. EIS is a technique where an excitation is applied, and the response is observed. The input and output signals can vary a lot, depending on final goals [26]. Usually, for corrosion evaluation purposes, the variation of the current in function of frequency is measured in response of a small sinusoidal perturbation of the potential [25]. Two are the main plots obtained, Nyquist plot (Z' vs Z'') and Bode plot (frequency vs phase angle and frequency vs impedance module).

EIS results can be better understood if the coating is represented through an equivalent circuit. Depending on the shown behaviour, the obtained curves from EIS can be related to circuit elements. Part of the EIS analysis is based on finding the equivalent circuit that best fit the obtained results.

An ideal coating, where there is no penetration of water or ions inside the coating, can be represented as a resistance and a capacitor in series (Figure 3).

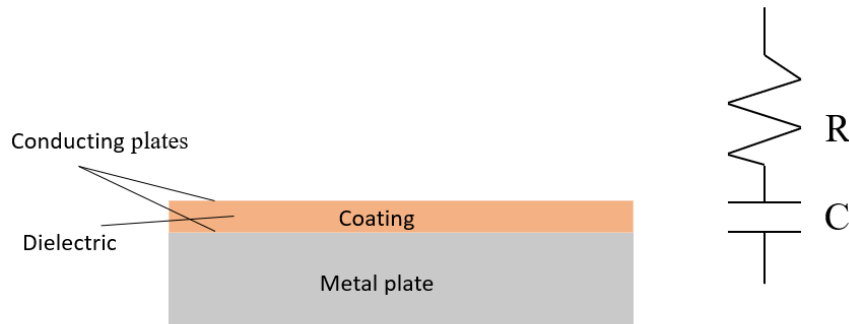


Figure 3: Ideal coating equivalent circuit

In this case R is the electrolyte resistance, that depend on ions concentration, types of ions and geometry of the area (Eq.11) [26].

$$R = \rho \frac{l}{A} \quad (11)$$

Where ρ is the resistivity, l is the length and A is the area.

The capacitor is mainly composed of two plates and a dielectric. In the case of an ideal barrier coating, the electrolyte and the metal surface represent the plates, while the coating is the dielectric [27]. The capacitance can be expressed with Eq. 12

$$C = \frac{\epsilon_0 \epsilon_r A}{d} \quad 12)$$

Where C is the capacitance, ϵ_0 and ϵ_r are the electrical permittivity and relative electrical permittivity, A and d are the area and the distance of the plates, respectively.

For a quasi-ideal coating, an equivalent circuit shows the electrolyte resistance, a capacitor, and a resistance for the coating (Figure 4). When, for example, ions reach the coating surface, the latter can act in two ways: either it blocks ions on the surface either ions penetrate in the coating. In this case the coating will show a capacitance (C_c) and a resistance, R_c . C_c is the capacitance of the intact coating, with values smaller than those of a double layer capacitor [27], while R_c represents the coating resistance to ion diffusion. The capacitor and resistance are in parallel since the coating cannot exhibit both behaviours at the same time.

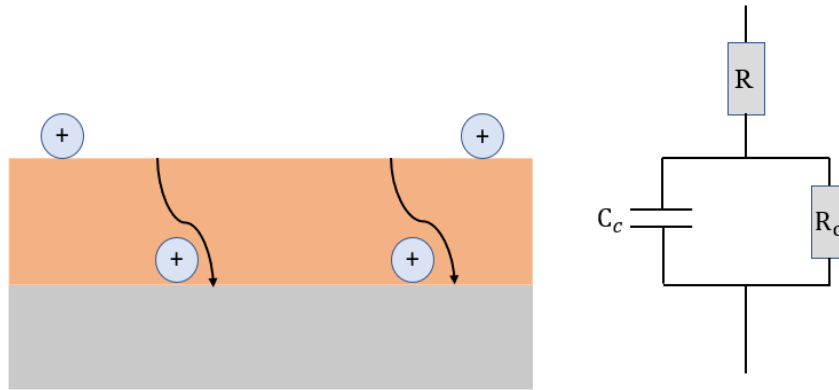


Figure 4: Quasi-ideal coating equivalent circuit

Figure 5 shows a Nyquist plot of a quasi-ideal coating [26]. This plot is shown as example to correlate equivalent circuit to actual EIS curves. Nyquist plot represents the real impedance vs imaginary impedance and does not show any dependence of values from the frequency. Nevertheless, usually high frequencies are represented on the left of the x-axis and low frequencies are represented on the right of the x-axis. The intercept of the curve with the x-axis at high frequency is the electrolyte resistance, while the intercept of the curve at low frequencies is the sum of electrolyte resistance and polarisation resistance [26]. It is important to notice that in practice usually only a part of the semicircle is obtained.

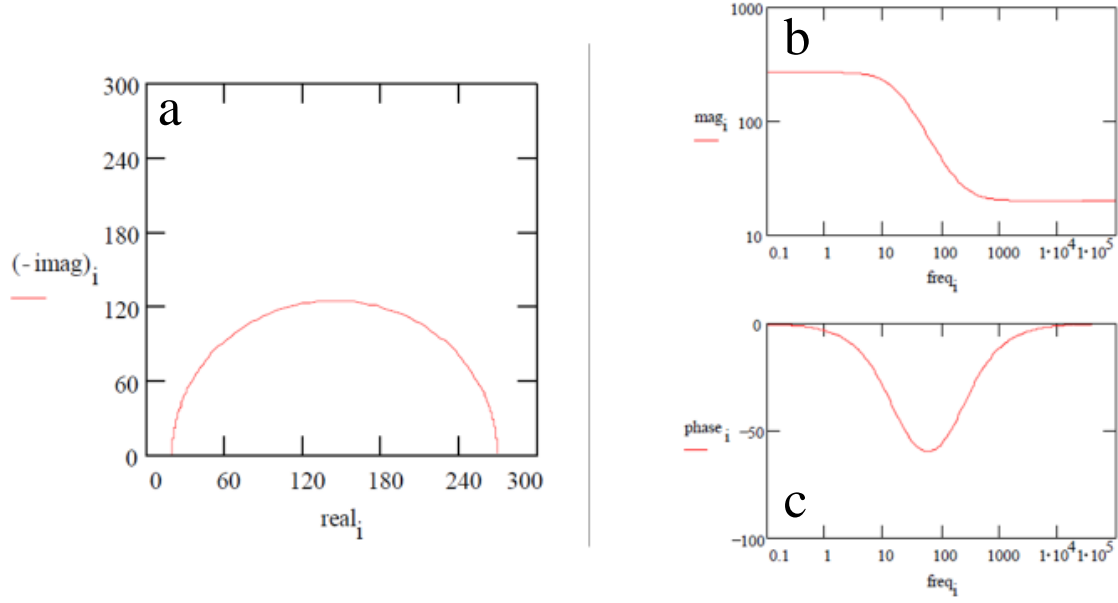


Figure 5: Nyquist (a) and Bode (b-c) plots of quasi-ideal coating [26]

The Bode plot in Figure 5 shows $|Z|$ vs. freq. (Figure 5b) and phase vs. freq. (Figure 5c). $|Z|$ is the summation of the modules of imaginary and real impedance, and it can be a useful tool when analysing EIS curves. $|Z|$ can be found in Nyquist plot if one imagines of drawing a vector from the origin of the axes to the circumference, as shown in Figure 6. ‘argZ’ is the angle between this vector and the x-axis, usually called phase angle [26].

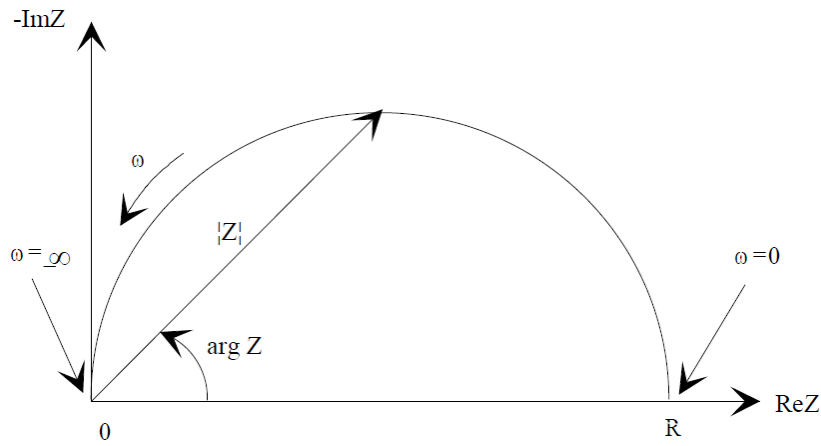


Figure 6: Nyquist plot example with representation of $|Z|$ and phase angle [26]

All coatings are expected to fail over time. Because of the presence of defects or because of porosity of the coating, water will reach the metal surface. In this case, the so-called failed coating, a new liquid/metal interface is formed (Figure 7). Despite the common agreement on the representation through the equivalent circuit proposed, its interpretation is still under debate [27].

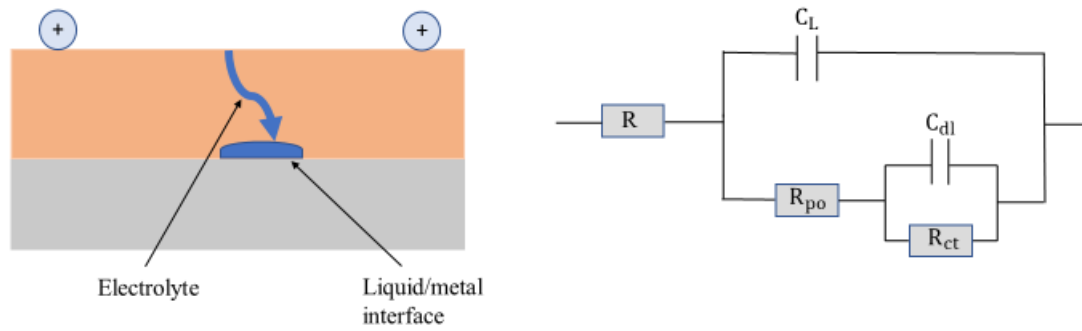


Figure 7: Failed coating equivalent circuit

In this representation C_L is the non-damaged coating capacitance, R_{po} is the resistance of pores, C_{dl} is the double layer capacitance at the liquid/metal interface and R_{ct} is the charge transfer reaction resistance. The circuit has the usual electrolyte resistance, R . The undamaged part of the coating shows the quasi-ideal behaviour, with a capacitor composed of two plates (electrolyte and metal) and a dielectric, the coating. When the electrolyte diffuses into the coating is subjected to a certain resistance of diffusion, the so-called pore resistance. Last, when electrolyte is accumulated on the metal surface, a double layer capacitor in parallel with charge transfer resistance is observed. The latter limits the kinetic of the reaction, that depends on many parameters, such as temperature and potential. The charge transfer resistance can be also written as polarization resistance, R_p . This is because the reaction that takes place shifts the potential from the equilibrium potential, the open circuit potential (OCP), when the cathodic and anodic reactions are in equilibrium, thus polarizing the electrode.

The proposed examples represent simple cases and in reality EIS curves are usually more complex. Nevertheless, these cases can work as a starting point to build a real-case scenario equivalent circuit and are useful to understand the theory this characterization technique is based on.

1.3 Chitosan

Chitosan can represent a breakthrough material for developments in new generation coating. Chitosan is a polysaccharide composed of D-glucosamine and N-acetyl-D-glucosamine. It can be easily obtained through partial deacetylation of chitin [28], a natural compound present in the shell of many crustaceous, as crabs and shrimps [29, 30], making it the second most abundant natural polymer on earth [31]. The chitin to chitosan modification is necessary to overcome some of the problem showed by chitin as low water solubility, that limit its spread and use. The deacetylation of chitin has the aim of removing the acetyl groups and freeing the amino groups, giving the polymer a cationic nature [32] (Figure 8).

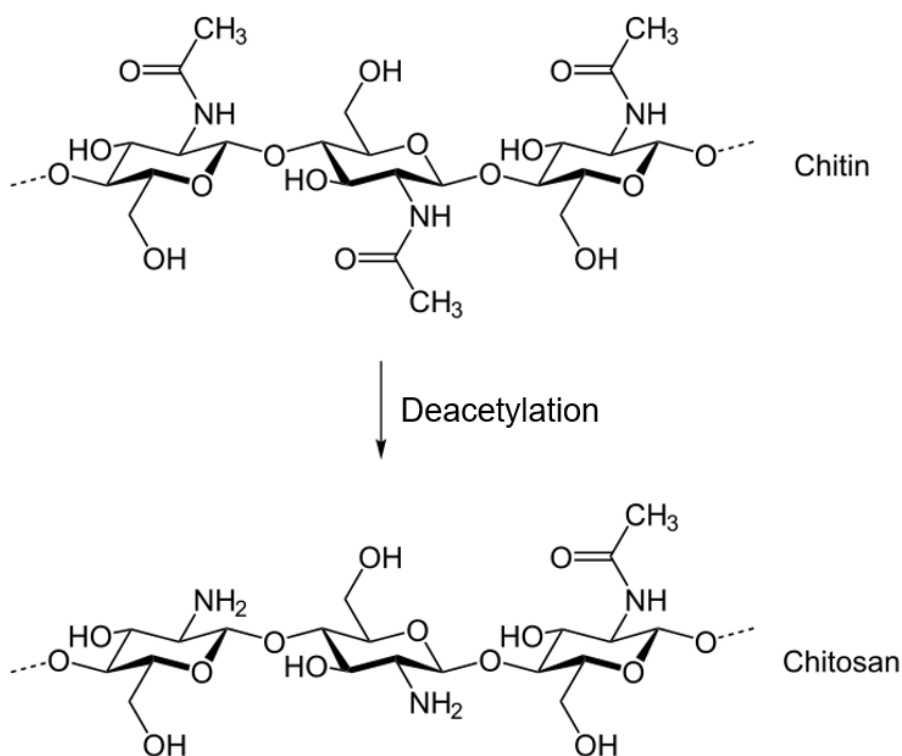


Figure 8: Deacetylation process [33]

The cationic nature is believed to be the reason of antimicrobial activity of chitosan, through interactions with the negative charges on microbial cell membrane [34, 35]. Other properties of chitosan are, for example, non-toxicity, biocompatibility and biodegradability [29], together with self-healing [36].

Self-healing properties of chitosan have been studied and applied to anticorrosive coating. Chitosan is usually added to epoxy to increase the already inherent ability of epoxy to self-heal [37]. Many strategies have been developed to improve self-healing ability of chitosan-based polymer, including dynamic covalent bonds and hydrogen bonds [24]. Dynamic covalent bonds, able to exchange or switch between several molecules [38], can break and reform in the damaged zones. One example of dynamic covalent bond is Schiff base linkage ($-\text{CH}=\text{N}-$). It can be created through the bonding of amino group of chitosan and an aldehyde group (for example glutaraldehyde) from another polymer [24]. In this case the self-healing properties of chitosan-based polymer depend on dynamic equilibrium of Schiff base linkage [24].

When in acid environment, chitosan is a polycation [24]. In this scenario, self-healing ability of chitosan-based polymer relies on strong hydrogen-bonding interactions [24].

Because of its polycationic nature in acid environment, chitosan is believed to be a good matrix for anticorrosion coating. The $-\text{NH}_3^+$ groups can bond OH^- generated by increase of pH due to corrosion neutralizing the pH of defected area [24]. Moreover, the penetrated water increases the mobility of CS chains, improving its self-healing action [24]. Chitosan is used in a wide range of other applications. Its good properties in terms of antibacterial protection make it suitable for food

industries [39, 40]. It can be used also for heavy metal removal [41], agriculture [42] and biomedical application [43].

Despite the above-mentioned properties and variety of applications, rarely chitosan is used alone. The downsides of chitosan, as poor mechanical strength [44], make unsuitable for many applications. This is the reason why chitosan is mainly used in composite materials to overcome its limits. Examples are the use of chitosan/sporopollenin for metal removal [41] or chitosan zinc oxide nanoparticles for prevention of marine biofouling [45] and food packaging [39]. Moreover, surface treatment through Poly(maleic anhydride-alt-1-octadecene) (PMAO) and Poly(ethylene-alt-maleic anhydride) (PEMA) [22] can successfully functionalize chitosan coating on metal surface to improve its properties as anti-corrosion barrier. In this case chitosan acts as physical barrier retarding diffusion of corrosive species.

Chitosan seems thus a very good candidate as polymeric matrix for a fully natural coating for corrosion protection. Not only it would allow for antimicrobial action and matrix for anticorrosive agents but would ideally ensure the self-healing property for a long lifetime coating. Through specific functionalization of the surface, moreover, it can act as active barrier against corrosive species diffusion.

1.4 Pollen

Pollen is a natural compound that is widespread all over the world. It is known that pollen is mainly composed of a hard exine (sporopollenin, cellulose, etc.) and a tender core, containing all the main nutrients [46]. Sporopollenin, the most studied component of pollen, has a controversial chemical composition because of its high resistance in degradation [47] that makes difficult its study. A recent study [48] indicates aliphatic-polyketide-derived polyvinyl alcohol units and 7-O-p-coumaroylated C16 aliphatic units as main components.

Despite the uncertainties around its chemical composition, pollen, in particular sporopollenin, has been recently used in a wide range of applications. Together with its bio-nature, its high porous structure makes it suitable for different uses (Figure 9). Hamad et al. [49] used sporopollenin microcapsules for the encapsulation of living cells. The partially permeable sporopollenin capsule walls allow for the migration of nutrients, making sporopollenin suitable as bioreactors. Another widespread use of pollen grain is as bio template. Examples of this application are the use of pollen to as bio template to produce hollow SiO₂ microspheres for further drug delivery system [50] and for the production of hierarchically porous NiO/C composite for lithium-ion batteries [46].

Because of the afore-mentioned properties, pollen is believed to be suitable as carrier agent of anticorrosion compound. The idea is that it is possible to load the anticorrosion agent into the pollen pores and, when cut, the anticorrosion compound will be freed and protects the metal surface from corrosion.

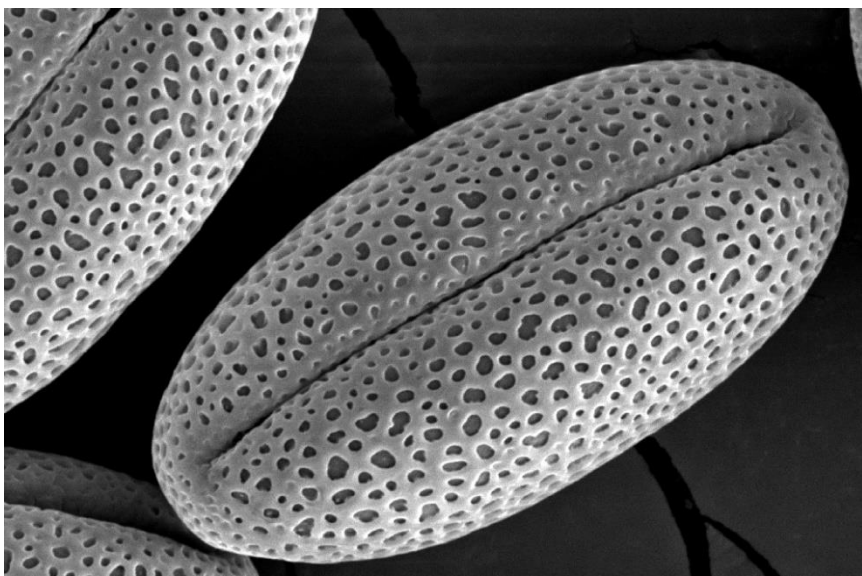


Figure 9: Pollen grain SEM image [51]

1.5 2-Mercatobenzothiazole

2-mercaptobenzothiazole (MBT) is a compound formed by a benzene ring fused with a mercaptobenzothiazole ring (Figure 10). Among other uses, as for vulcanization of rubber [52], MBT has been widely used as corrosion inhibitor for different kind of metals, such as copper or carbon steel [23, 53].

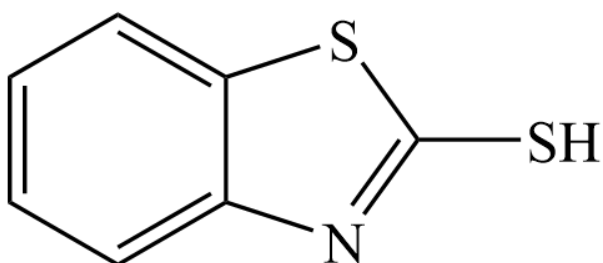


Figure 10: Chemical structure of MBT

MBT inhibition action is due to its chemical reactivity with metals. MBT chemically bond with metal through the metal-sulphur bond, creating self-assembled monolayers (SAM) [54]. The rest of the MBT structure creates a packed and hydrophobic monolayer, that prevents water to come into contact with metal and thus inhibiting corrosion [55].

Figure 11 shows the release profile of MBT in different pH conditions [23]. No clear difference is noticeable when comparing pure water and NaCl water solution, while much higher release rate is observed in acid and basic environment. The release profile of MBT is very interesting since it influences the working environment and the process design of MBT-containing solutions.

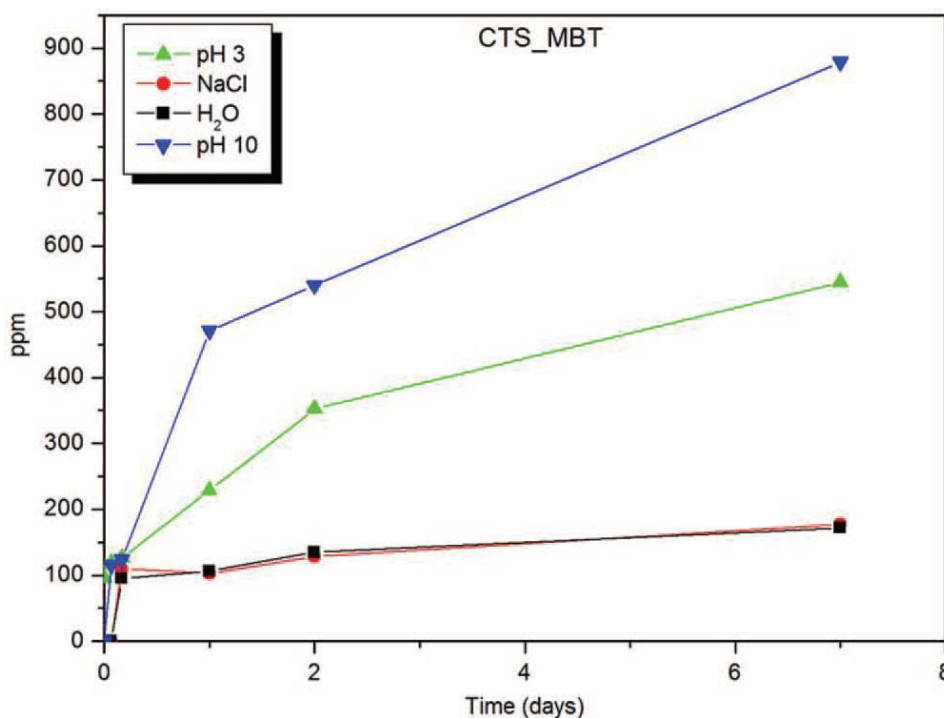


Figure 11: Release profile of MBT from CS-MBT in different conditions [23]

MBT seems thus a good candidate as active corrosion inhibitor agent. It has been already used as metal anticorrosion inhibitor [23, 56] also in controlled release coating with chitosan matrix [23], showing high compatibility since the lack of side reactions. Moreover, its theoretical hydrophobic behaviour should be suitable for water environment and its dispersion in water and seawater environments looks suitable for long-time application.

1.6 Biofouling

Biofouling is defined as the accumulation of macro and micro- organisms on wetted surfaces. Biofouling becomes particularly damaging when it occurs on surfaces that have a mechanical function limiting or damaging its action and it represents a worldwide problem in aquatic industries. On ships, for example, it can reduce the manoeuvrability, as well as the speed, increasing fuel consumption and maintenance cost while on static structure it can lead to mechanical failure or speed corrosion mechanism [57]. Marine biofouling starts immediately after the immersion of the interested part in water [57] and most of the anti-biofouling techniques have the aim of avoiding the cell adhesion and to kill approaching organisms [58].

Biofouling process usually starts with microorganisms that colonize surfaces, followed by sequester of nutrients from water to transform them in metabolites and new biomass [58, 59]. Industrial systems usually offer large areas which are often colonized, affecting the producing rate and quality [59]. Many factors have been indicated as biofouling film influencing factors, as temperature, nutrient availability, flow velocity, physical and chemical characteristic of the substratum and suspended

solids [59]. The control of these factors can somehow limit biofouling film creation, while other preventions methods, as treatments with biocides and antifouling coating, can be successfully used to further increase the antifouling action.

As mentioned in the previous section, state-of-the-art anti biofouling coatings release toxic species in the marine environment [60], and always more countries started acting limiting the use or the concentration of toxic paints. Three are the major mechanisms the last years developed anti-biofouling coating are based on: prevention of attachment to surface by micro and macro organisms (*fouling-resistant coatings*), reducing biofoulants sticking strength (*fouling release coating*) and the destruction of biofoulants (*fouling-degrading coatings*).

Fouling-resistant coatings mechanism relies on the surface energy between water and the coating. Two major classes of coatings have been recognized: hydrophobic surfaces, known for good 'fouling release' ability, and hydrophilic, where no attachment on surface is detected [61]. Non-polar hydrophobic surface, for example, shows high polymer – water interfacial energy. In this case, biomolecules as proteins tends to be absorbed to minimize the interfacial energy [61]. On the contrary, on hydrophilic surface the adsorption of biomolecules wouldn't lead to any significant advantage in terms of reduction of interfacial energy, and thus these surfaces shows good resistance of adsorption [61].

Fouling release coatings, mentioned in the above paragraph, have the ability of minimizing the adhesion between coating and organism, allowing for hydrodynamic stress or simple cleaning as an easy removal of fouling organisms [62]. Biocides free polymers used for fouling release coatings have low surface energy and low modulus (E) [58].

Fouling-degrading coatings are simply based on the concept that some polymers have an antimicrobial activity. The charge distribution over the polymeric chain allows for the degradation of microbials. Cationic polymers with quaternary ammonium compounds are the most common polymeric class used for this purpose [58]. The antimicrobial activity is due to electrostatic interactions between the cationic head of the ammonium compound and the negative bacterial membrane; the polymeric chain penetrates into the intermembrane region, degrading the bacterium [63].

Most of the effective anti-biofouling paints contains tributyltin (TBT) that is an environmental harmful chemical. The ban of TBT-based paints led to major changes in antifouling paint industries [64]. Despite some good accomplishments in anti-biofouling coatings without toxic compounds have been obtained [45, 65], there are no very effective fouling protective coating available on the market that are 100% not toxic. Most of the marine antifouling paints include Cu(I)- based biocidal pigment [60], a toxic material to marine organisms [58]. ZnO is sometimes used as well, mostly together with Cu(I) as booster, and thus increasing its toxicity [66]. Other toxic compound can be used for some other more resistant algae [60].

Despite in the past zinc oxide has been used as support for other materials as Cu(I), recent developments in antibiofouling technology led to a focus on zinc oxide nanomaterials as active antifouling material, as described in the next section.

1.7 Zinc oxide nanoparticles

One of the most common way to ensure antimicrobial and antibacterial activity of chitosan coating is the use of oxide agents, metal nanoparticles or conductive polymer [67]. Among the others, zinc oxide (ZnO) has recently attracted interest because of its low cost, low toxicity and antimicrobial activity [68]. Moreover, it has been defined a safe material [69]. ZnO is an antibacterial material since it exhibits antibacterial activity without the presence of light [70], probably due the production of hydrogen peroxide from its surface [71]. The high antibacterial activity is due to its semiconductor nature that allows for photocatalytic behavior. The incident light excites electrons in the valence band and promotes their excitation to the conduction band. The electron-hole pairs are separated to the surface, where they react with the surrounding producing reactive radicals (Figure 12). The use of nanoparticles (NPs) should allow for selective absorbance of visible light due the presence of intrinsic electron defect states. Both ZnO nanorods [72] and nanoparticles [45] were successfully used with chitosan in anti-biofouling applications in marine environment. Together with its semiconductor nature, the antibacterial activity of zinc oxide is also due to destabilization of bacterial cells through direct contact with zinc oxide walls and to anti-bacterial properties of Zn^{2+} ions released by ZnO in aqueous environment [73].

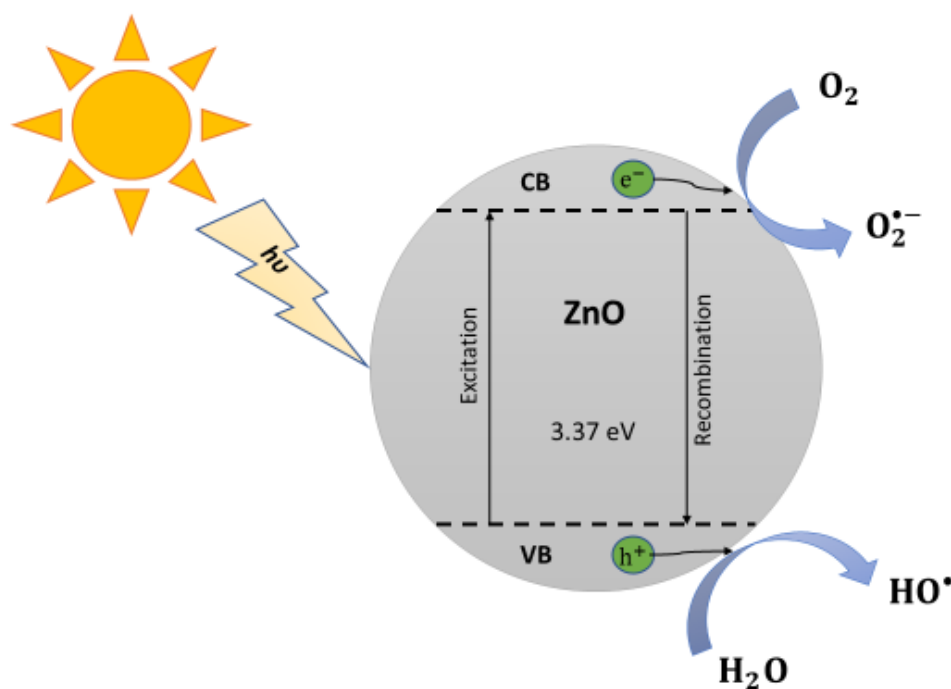


Figure 12: Schematic mechanism of photocatalysis of ZnO

1.8 Objective of the thesis

The scope of the work is to combine the properties of chitosan material, as self-healing and anti-biofouling, with the high theoretical entrapping properties of pollen. The theoretically high porosity of pollen and its bio-nature makes it very attractive as entrapping agent for bio-based material for corrosion protection.

In particular, the aim of this study is to develop a fully natural polymer with triple action:

- Anticorrosive
- Self-healing
- Anti-biofouling

Ideally, the active anticorrosion activity is given by the chitosan matrix as active barrier between the metal surface and the environment, while the passive anticorrosion activity is given by the MBT entrapped into pollen grains and released when the coating is scratched. The self-healing property is achieved thanks to the chitosan matrix, while the anti-biofouling action is provided by the ZnO NPs.

Particularly important is the fully sustainable composition of the coating. As already mentioned in the state-of-the-art coating section, nowadays most of the them have heavy metals composition, and with the always more increasing importance of pollution-related problems, it is just a matter of time that coating themselves will be appointed as one of the factors that increase pollution. The 100% natural composition of the coating can be considered as the fourth aim that, together with the aforementioned ones, this ambitious project has.

2 EXPERIMENTAL

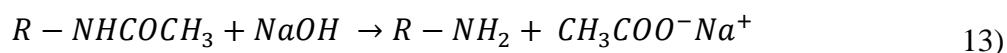
2.1 Materials

Stainless steel plates were received by Slöjd-Detaljer AB, Sweden, in dimensions of 250x500 mm with a thickness of 0.5 mm. They were cut into 1x1 cm squares for subsequent treatments. Chitosan (molecular weight 100,000-300,000) was purchased by Acros Organics. Sodium hydroxide (NaOH), Glutaraldehyde (GA) 25% solution in water, Dichloromethane (DCM) and buffer solution pH=11 were purchased by Merck KGaA Darmstadt, Germany. Poly(maleic anhydride-alt-1octadecene) (PMAO), 2-Mercaptobenzothiazole (MBT), 11-mercaptoundecanoic acid (MUA), 1-ethyl-3-(3-dimethylaminopropyl)carbodiimide hydrochloride (EDC), N-Hydroxy-succinimide 98% (NHS), Acetic acid and Zinc oxide NPs dispersion 50wt% in water were bought from Sigma-Aldrich Chemie GmbH Steinheim, Germany. Bee pollen powder was purchased by BulkPowder.com Colchester, UK. Oleic acid (OA) was purchased by VWR Chemicals, Fontenay-sous-Bois, France and Ethanol was bought from Solveco Rosersberg, Sweden

2.2 Methods

2.2.1 Deacetylation of chitin

As anticipated in section 1.3, the deacetylation of chitin is a fundamental process to modify the chitin molecule into chitosan one, changing its properties to make it suitable for many applications. The deacetylation process allows the acetyl groups (-COCH₃) to leave to free amino groups (-NH₂), according to Eq. 13 [74]:



The degree of deacetylation (DDA) is of outmost importance to establish the purity of chitosan. In fact, it allows for a more precise understanding of the involved molecules and for a better prediction of the molecule behavior. Depending on the degree of deacetylation, for example, chemical activity of chitosan can be changed through a different amount of available amino groups.

Chitin deacetylation process was carried out partially following the procedure described in [28]. A 40% NaOH in water solution is prepared. Then, 3.5 g chitin are added (1:20 volume ratio solid/solvent). Solution is stirred until it reaches homogeneity and it is then poured in the autoclave (100 mL). The autoclave is placed in the oven at 150°C for 2 h. When finished, the solution is filtered and washed until neutral. Chitosan is then dried at 40 °C under vacuum condition overnight. The deacetylation reaction can be described as in

An autoclave has been used to allow for increase the rate of the reaction and to thus to allow for a faster deacetylation [28].

A first test on deacetylation of chitin, carried out following more carefully the procedure described in [28], was done prior to the deacetylation experiment described above. In the first test, a 1:10 solid

to solvent ratio was used, temperature was set at 120 °C and the time spent in oven was of 1h instead of 2. The reason this method was changed is that it resulted in a lower deacetylation degree than expected (results not shown).

2.2.2 Pollen

Pollen first treatment is done in order to clean it from impurities and to wash away all the nutrients contained inside the pollen grains, to free space for MBT loading. The followed procedure is very similar to the one adopted in [50]. In particular, 5% pollen in ethanol solution is sonicated through probe for fifty minutes. The solution is then centrifuged at 10000 rpm for ten minutes and the pellet is re-dispersed in ethanol (5% solution). Sonication through probe is performed again, with following centrifuge. The pellet is then dried at 40°C under vacuum conditions overnight.

For the sake of completeness, another pollen treatment was tested, partially following the procedure described in [46]. To this end, 5% w/v solution of pollen in ethanol is prepared. The solution is sonicated with pulse mode for 30 minutes through probe. It is then centrifuged for 10 minutes at 10000 rpm. Ethanol is removed and new ethanol is poured in the vials and pollen is re-dispersed. Solution is then poured in a new beaker. Then, it is sonicated for 30 minutes with pulse program. Again, centrifugation is carried out. Meanwhile, a solution 1:1 V ethanol and formaldehyde (37% in water solution) is prepared. Pollen is poured in the new solution and it is stirred under fume hood for 10 minutes. The solution is washed and dried in oven under vacuum (0.15 bar) for 12 h 40°C. Pollen is then grinded. No clear differences arise from the SEM images of pollen obtained with the two methods (Figure 23 in Results section) and thus the faster and easier method, the first described, is chosen.

In order to make pollen suspended for enough time for following treatment, it is left reacting with oleic acid. Oleic acid should improve the suspension stability of pollen [75]. A 14% pollen in oleic acid solution is prepared. Meanwhile, a boiling flask is immersed in oil bath, and a condenser tube is connected with water in and water out tubes for water recirculation. 70 mL of water are poured in the boiling flask, and temperature is raised to 110 °C. Magnetic stirring occurs both in the oil bath and inside the boiling flask. When 110°C is reached, the pollen in OA solution is poured drop by drop. Solution is left stirring under reflux condition for 1 h. The left solution is centrifuged and washed with ethanol. It is then washed with dichloromethane (DCM, CH₂Cl₂) and then left drying overnight.

2.2.3 Phase transfer and cross-linking

Pollen-OA and PMAO, in the same weight ratio, are mixed in DCM (pollen 2% in DCM) until complete evaporation of solvent. 20 mL of buffer solution at pH=11 are then added and the solution is sonicated with probe for 50 minutes. The reason is that PMAO molecule in basic environment opens the ring and creates carboxyl groups (Figure 13). Solution is then centrifuged and the washed with water. The remain pellet is re-dispersed in water and 0.2 mL of MBT in acetone (10%) are added. Solution is stirred for 1 hour and half and is then centrifuged and washed with water. Pellet is re-dispersed in 8 mL water and EDC and NHS are added (39 mg and 115 mg respectively) to allow for

crosslinking (Figure 14). In the procedure, EDC/NHS coupling agents are used to crosslink PMAO to chitosan through carboxyl groups of PMAO and amino groups of chitosan.

First attempts in polymer production resulted in a lack of MBT loaded into pollen. The difference with the above-mentioned method was the order some procedures were carried out. MBT was in fact loaded prior to PMAO treatment and buffer solution addition. As shown in Figure 11 in section 1.5 in the introduction part, MBT is easily released in basic environment. The treatment with buffer solution at pH=11 most likely was the cause of the lack of presence of MBT in the final polymer. Thus, PMAO addition and buffer solution treatment were carried out prior the MBT loading.

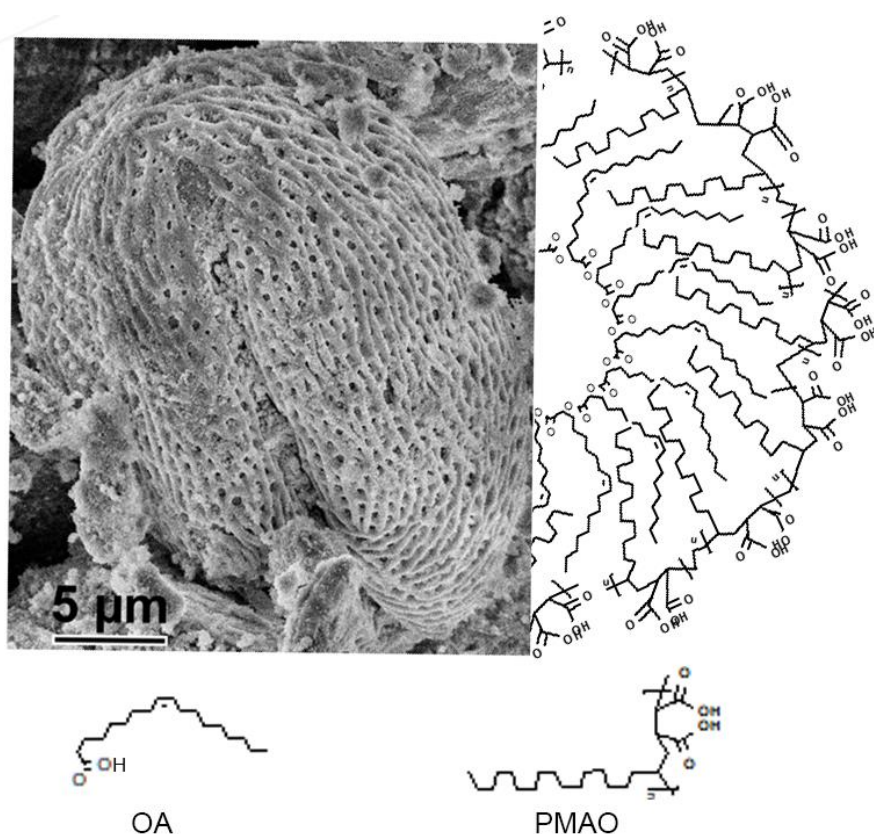


Figure 13: Schematic representation of pollen, OA and PMAO system

Technically, EDC alone could be used to crosslink carboxyl groups to amino groups of chitosan. Nevertheless, NHS addition make the NHS ester more stable compared to the intermediate product produced with EDC alone [76](Figure 14).

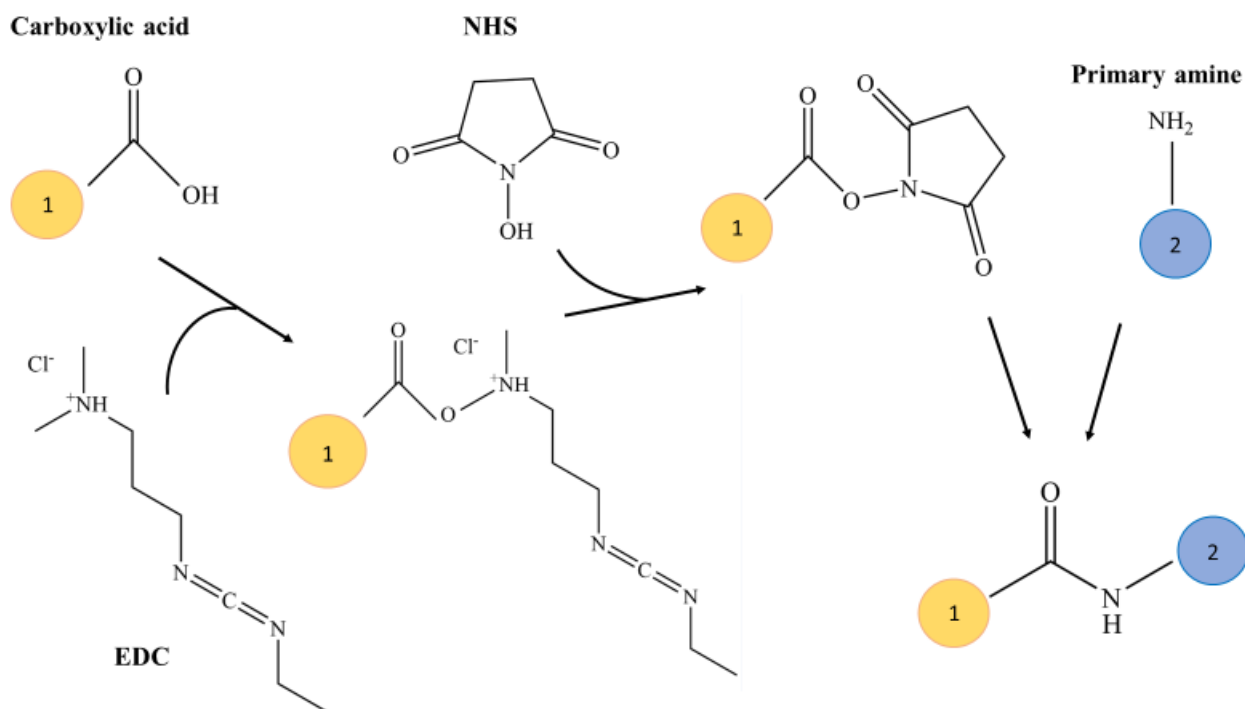


Figure 14: Schematic representation of EDC/NHS crosslinking

In Figure 14, in our experiment 1 stands for pollen-OA-PMAO and 2, with amino groups, represents chitosan.

Meanwhile 100 mL solution 1% acetic acid is prepared, and pH adjusted to 4.5 though NaOH 1M solution. Chitosan is then added (1%) and solution is stirred for 1 h. ZnO NPs dispersion (50wt% in water) is added (5 wt% to CS). The two solutions are then mixed together and stirred for 2 h. Last, GA is added (9% to chitosan) to allow for partial crosslinking of chitosan chains. GA has two terminal carboxylic groups that bond with amino groups of chitosan forming an imine bond ($-C=N-$) [77, 78](Figure 15). Many different combinations can be obtained adding GA to chitosan: GA can link amino groups of the same polymeric chain or from different chains (intra- and inter-), and different GA chains can be linked together and only further be linked to amino groups.

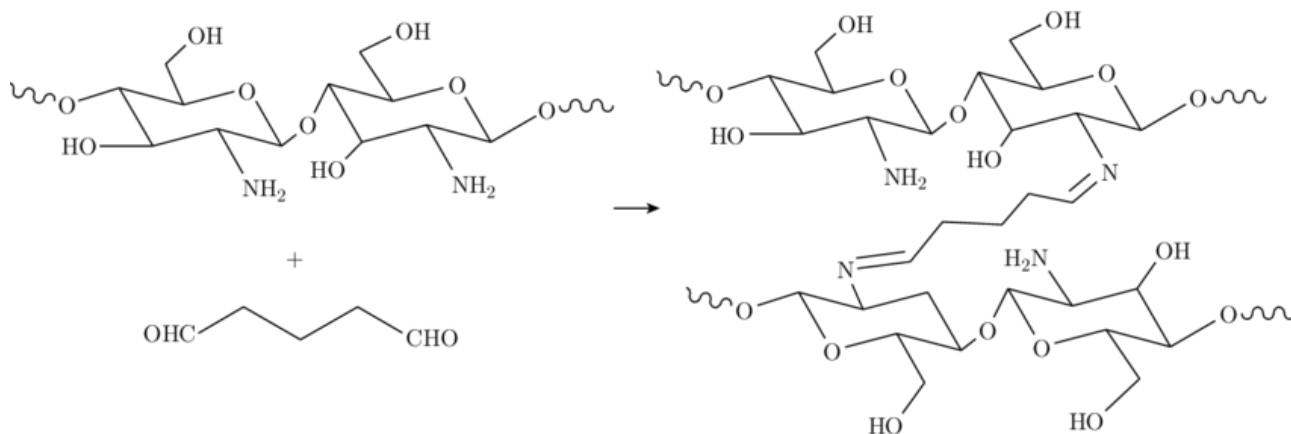


Figure 15: Schematic illustration of chitosan-glutaraldehyde crosslinking mechanism [79]

The right amount of GA has been found with a simple trial and error approach. GA amounts of 12 and 10% with respect to chitosan resulted in a too high viscous polymer, impossible to be applied through spray coating. GA amount of 7%, on the contrary, resulted in a too low viscous solution with low pollen suspension. Last, GA amount of 9% with respect to chitosan showed the best tradeoff between pollen suspension and spray ability.

Two reference solutions are also prepared to compare the results with. The reference solutions are prepared with 1% chitosan in 1% acetic acid solution in water. GA (3 and 7 wt% to chitosan) is added to give the polymers a good viscosity. The solutions will be applied as the main solution, with the steps described below in section 2.2.4 and 2.2.5.

2.2.4 Surface preparation

Metal samples of 1x1 cm dimensions were mounted on phenolic support through SimpliMet 4000 Automatic Compression Mounting System. Heating time was set at 4:30 minutes at 180°C, and the used cooling time was 2:30 minutes. The applied pressure was 290 bar.

Grinding of the samples was done through Buehler Alpha 2 speed grinder-polisher machine. Stainless steel plates were grinded with CarbiMet silicon carbide grinding paper (grit P320, P600, P1200, P2500 and P4000 in sequence) for 1:30 minutes at 20 N applied force to obtain a mirror-like surface.

Before application of the coating, a primer layer is applied. 2-mercaptopundecanoic acid was chosen as previously reported as successful primer for metal surfaces as gold [80] and stainless steel [81]. It can be applied through different methods, as simple dip coating at room temperature [82]. In this work, self-assembled monolayer (SAM) of MUA was formed onto stainless steel plates through dip coating under reflux condition in a 10 mM MUA in ethanol solution, for 6 h at 95 °C. Ideally, MUA should link to stainless steel through Fe-S covalent bonding, leaving a carboxylic group at the other extremity of the chain to further link to chitosan through amino groups. After reflux, samples are rinsed with ethanol two times and then dried under vacuum at 40°C for 1 h.

2.2.5 Coating methods and surface coating

Several techniques are available to apply the coating to the metal surface. Three of these techniques were considered: brush coating, dip coating and spray coating [10]. Brush coating, despite the ease of application, would result in a too inhomogeneous coating. Dip coating would probably be the best in terms of homogeneity of coating. Nevertheless, long application times are required for dip coating. Moreover, being the aim of this thesis project to be a first step in a further development of this technology, dip coating would not be suitable for large scale applications. Last, spray-coating represents a good compromise between ease of application, short application times and homogeneity of coating. Moreover, when compared to dip coating, spray coating techniques results in better results for coating application for anticorrosive purposes [83].

Spray coating of the polymer was performed with Iwata Hi-Line HP-TH Gravity Feed Dual Action Trigger Airbrush. Layer-by-layer (LbL) assembly technique was used, with an average of 5 µm thickness coating for each step.

A few tests have been carried out to topcoat the coating to ensure hydrophobic behaviour. To this end, two different solutions were adopted. With the first one, a stearic acid (SA) 0.1M in tetrahydrofuran (THF) solution is spray coated with a three-steps coating for a total topcoat thickness of 6 μm . The second top coating uses a PMAO solution 0.1 M in toluene with a three-steps coating though spray coating [22]. The effect on hydrophobicity of the topcoat is showed in contact angle paragraph (3.6.4) in the Results section. PMAO is supposed to improve the hydrophobicity of the coating because of its aliphatic structure at the coating/solution interface [22], while stearic acid is believed to attach to chitosan through the carboxyl group, exposing the hydrophobic chain and thus increasing hydrophobicity.

Different tests have been carried out before deciding which deposition method was the most successful. The first test was carried out without primer. The lack of use of primer brought to inhomogeneous coating. After the first attempts, tannic acid was chosen as primer since it is believed to be a good candidate to link to both stainless steel (SS) [84] and to chitosan though its numerous OH groups [85, 86]. After the first experiments tannic acid was believed not to be successful because of bad attachment shown by the coating to the metal plate by SEM images (Figure 27a in results section). Nevertheless, further analysis on coating attachment led to the idea that the cross-section preparation might influence the quality of attachment detected by SEM. Thus, tannic acid was further used, and cross section analysis was carried out though optical microscope (Figure 31 in Results section) showing good results in terms of surface attachment. Different tests were also carried out on how to apply the primer (dip coating, spray coating or brush coating) and how to apply the coating (spray coating, drop coating and brush coating). No clear differences arise from the comparison of dip and spray coated primer (results not shown) while brush coating, for both primer and coating, resulted in a too inhomogeneous coating. This multiple application tests of primer and coating suggested that spray coating is the most suitable technique to apply the coating, while primer can be applied both though dip coating or spray coating. Nevertheless, spray coating has the great advantage of time saving, thus being preferable over dip coating.

The influence of polymer morphology was also considered. Pollen grains, in fact, with an average dimension of 20 μm , are believed to be possible obstacles to good attachment of the coating to the metal surface. To overcome this problem, a first layer of bare chitosan crosslinked with GA 3% is applied until a thickness of around 15 μm is obtained. Then, the composite is applied as normal.

Last, different tests were carried out with surface preparation. As mentioned in section 1.2.4.1 in the introduction part, surface preparation is of outmost importance for a good attachment of the coating to the metal surface. Despite literature suggests the use of mirror-like surface, a coarser grinding would result in mechanical bond of coating to the surface. Thus, a coarser grinding obtained with CarbiMet silicon carbide grinding paper (grit P320 and P600) was tried.

2.3 Characterization

2.3.1 Material characterization

2.3.1 Degree of deacetylation evaluation

The degree of deacetylation is determined through the first derivative of UV-Vis spectrometry [87], since it represents a fast and precise method of evaluation when compared to other methods, as titration method [28] and FT-IR. In particular, the absorbance of N-acetyl-D-glucosamine (non-deacetylated monomer of chitosan) has been demonstrated independent on the acetic acid concentration at particular wavelengths, thus giving precise results on the DDA for 199 nm wavelength. First, a calibration curve with different concentration of N-acetyl-D-glucosamine (0.005, 0.01, 0.015, 0.02, 0.025, 0.03, 0.035, 0.04 mg/mL) in 0.01 M acetic acid is made. Then, a UV-Vis analysis on chitosan solution (0.1 and 0.05 mg/mL) in 0.01 M acetic acid is performed. Once the relative N-acetyl-D-glucosamine amount is determined for the deacetylated chitosan, the degree of deacetylation can be established with the following equation [88]:

$$DDA = \left(1 - \frac{C_g}{C_i}\right) \times 100 \quad 14)$$

Where C_i is the initial chitosan concentration and C_g is the N-acetyl-D-glucosamine relative concentration.

2.3.2 2-Mercaptobenzothiazole amount evaluation

MBT (2-Mercaptobenzothiazole) is used as anticorrosive agent loaded into pollen grains, as explained in the polymer production section. MBT shows a characteristic peak in the UV-Vis spectrometry at 320 nm [89]. In order to evaluate the loading efficiency of MBT in pollen grains, first a calibration curve is obtained. Different amount of MBT in ethanol (0.0002%, 0.0005%, 0.001%, 0.0015% and 0.002%) are analyzed and a linear regression of their peak heights is obtained. The UV-Vis spectra of the final polymer will show a characteristic peak at 320 nm. Through the obtained calibration curve and through simple algebraic passages, considering dilutions and the total volumes involved, the amount of MBT in the polymer can be established, and comparing it with the total MBT amount used the loaded percentage can be extrapolated.

2.3.3 Viscosity

Viscosity is an important parameter when dealing with polymer. Viscosity will influence both the easiness of spraying the composite and its performances. Dynamic viscosity is measured with a rotational viscometer ViscoQCTM100-L, Anton Paar Nordic AB, Malmö, Sweden. For the measurement, a measuring bob and a measuring cup for small volumes are used. The TruMode is set to have the measurement at a torque of around 80%. Moreover, an average value out of three measurements with standard deviation is considered as final result.

2.3.2 Characterization of coating

2.3.2.1 Thickness

Thickness is evaluated through Coating Thickness Gauge CM10 series by Yushi Instruments. It allows for a preliminary evaluation of thickness for both ferrous and non-ferrous materials. A more precise evaluation of thickness is available through SEM analysis of the samples' cross-sections. As for viscosity, three measurements all over the surface are done and the mean value is considered.

2.3.2.2 Coating morphology

Optical microscope (OM) images were taken with Leica DM LB microscope. The purpose of the microscope is a preliminary analysis of the surface, with the aim of analyzing the surface homogeneity and the eventual presence of impurities.

SEM (FE-SEM, Zeiss GEMINI® Ultra 55) was used to further analyze the samples morphology. Both the cross-section and the plane surface were analyzed. Cross-section analysis was performed to evaluate the quality of attachment of the coating to metal surface, while surface analysis was conducted to seek for any cracks or impurities.

In SEM, an electron beam, usually generated by tungsten filament, hits the sample producing different types of signals, as secondary electrons (SE), backscattered electrons (BSE), X-rays and Auger electrons, depending on the occurring interaction. These different signals are collected by detectors and they are then transformed into a signal that is transformed into images in the monitor (Figure 16). The main source of information in SEM are SE and BSE. SE have lower energy with respect to BSE and they are generated by anelastic interactions between high energy incident electrons and valence electrons of sample's atoms. BSE, on the contrary, are generated by elastic interactions between incident electrons and the sample's atoms' nuclei, and they are characterized by high energy. BSE emerge from deeper regions in the sample while SE emerge from the contact point of the electron beam and the sample's surface and are thus used for surface analysis.

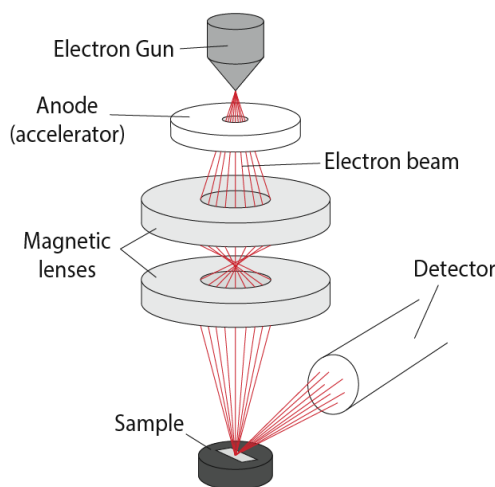


Figure 16: SEM schematic representation [90]

2.3.4 Evaluation of properties

2.3.4.1 FT-IR

FT-IR (Thermo Scientific Nicolet iS10 FT-IR Spectrometer) was used multiple times to evaluate step-by-step the coating composition. Attenuated total reflectance (ATR) mode was used.

FT-IR spectroscopy is based on the concept that different molecules have different vibrational frequency. When an electromagnetic wave in the IR spectra hits the sample, if the frequency of the input IR signal coincides with the vibrational frequency of the molecule, the incident signal will be absorbed. FT-IR characterization technique will thus result in an absorbance or transmittance peaks spectra, based on which chemical bond and molecule is present in the sample. Fourier transform (FT) means that a Fourier transform is needed to convert raw data into the actual spectrum. ATR is a specific mode of FT-IR analysis that uses total internal reflection that results in an evanescent wave. The IR light beam passes through the ATR crystal, being reflected (Figure 17). Reflection is not total, and an evanescent wave goes into the sample. Here it can be absorbed, resulting in a loss of energy of the beam that can be detected, or not, thus going back. Penetration depth varies usually from 0.5 to 2 μm

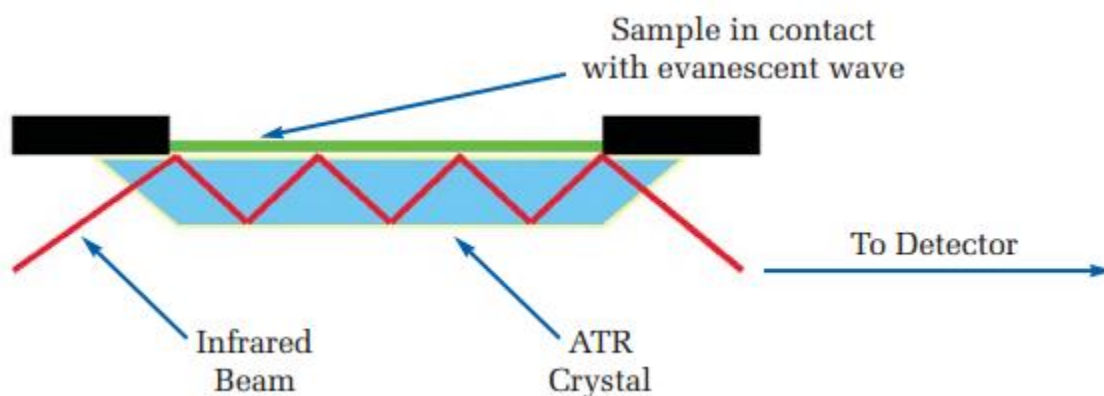


Figure 17: Schematic representation of FT-IR, ATR mode [91]

2.3.4.2 Hydrophobicity

An Ossila Contact Angle Goniometer was used for water contact angle measurement. The importance of contact angle in establishing the hydrophilic or hydrophobic behavior of the coating is explained by the aqueous environment the coating needs to work in. Thus, the more the hydrophobic behavior, the better it is. Contact angle tests were carried out all over the samples' surfaces and a mean value out of three measurement is considered.

2.3.4.3 Corrosion

Corrosion measurements can be carried out through EIS (VistaShiledTM Faraday Cage and Interface 1010ETM potentiostat, Gamry Instruments).

2.3.4.4 Self-healing

Since the lack of standard evaluation technique for self-healing coating, EIS can be used for self-healing ability evaluation purpose [92]. The main idea is to observe the polarization resistance over time. If an increase of the polarization resistance is observed, it is an indicator of self-healing capability of the coating [93]. Despite the good hints that EIS measurement can give on self-healing properties of the coating, there are three different mechanisms that can contribute to an increase of impedance: the oxide layer formation proper of stainless steel, the self-healing chitosan and the protective action of MBT on the scratched surface, as per our hypothesis. OM, as well as SEM and FT-IR can be implemented in the study of self-healing properties, giving some hints and more precise justification of which of the mechanisms is happening, if not a combination of the three.

3 RESULTS AND DICUSSION

3.1 Degree of deacetylation

First, the calibration curve is obtained by using different amount of N-acetyl-D-glucosamine as mentioned in paragraph 2.3.1. The first derivative curves for N-acetyl-D-glucosamine are shown in Figure 18.

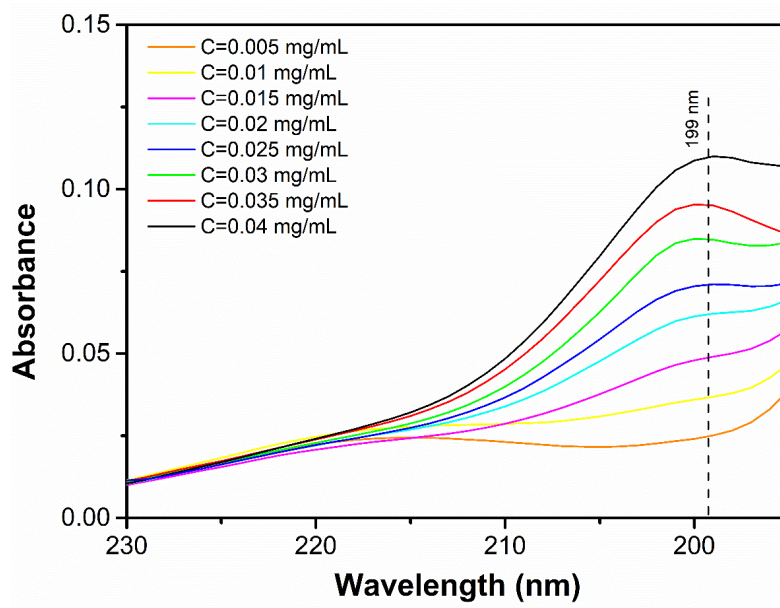


Figure 18: First derivative curves for different N-acetyl-D-glucosamine concentrations

The absorbance peak values for different N-acetyl-D-glucosamine amounts at 199 nm wavelength are listed in Table 1. Results show the mean value out of three measurements.

Table 1: Absorbance peak values at 199 nm for different N-acetyl-D-glucosamine concentrations

C [mg/mL]	0.04	0.035	0.03	0.025	0.02	0.015	0.01	0.005
H value (199 nm)	0.11 ± 0.0216	0.095 ± 0.00712	0.085 ± 0.00638	0.065 ± 0.00424	0.062 ± 0.00245	0.049 ± 0.00432	0.037 ± 0.00283	0.025 ± 0.00245

A linear regression of the peaks' heights (Figure 19) can be used for the following determination of DDA during the experiments.

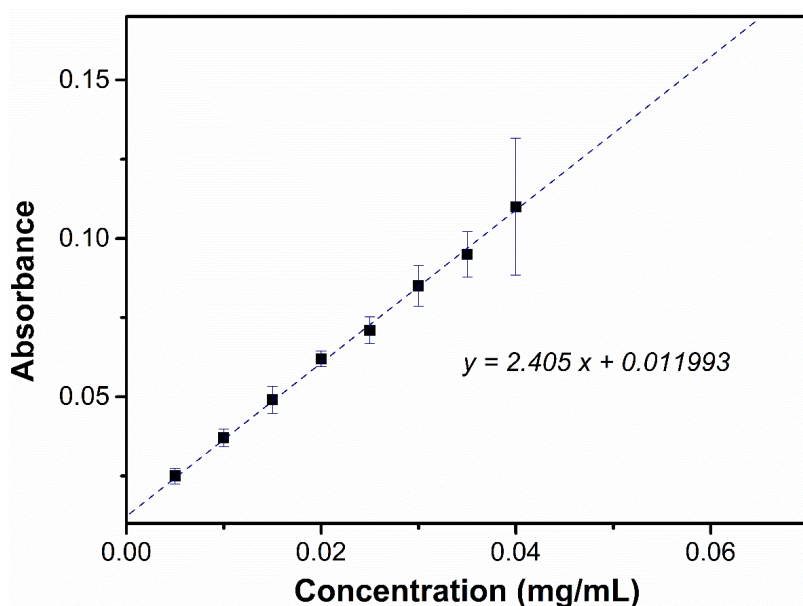


Figure 19: Peak heights at 199 nm for different N-acetyl-D-glucosamine concentrations, fit plot and linear regression

The deacetylated chitosan shows absorbance peaks equal to 0.02696 and 0.020635 for 0.1 and 0.05 mg/mL, respectively. Through the equation shown in Figure 19 the relative N-acetyl-D-glucosamine amount is calculated as 0.00622 and 0.00359 mg/mL, for a final DDA (through Eq. 14 above) equal to $93.3 \pm 0.48 \%$. This result is in accordance with the literature [28] and is considered a very positive result for the following tests.

3.2 2-Mercaptobenzothiazole content

First, the calibration curve is obtained by using different amount of MBT in ethanol. The curves for MBT are shown in Figure 20

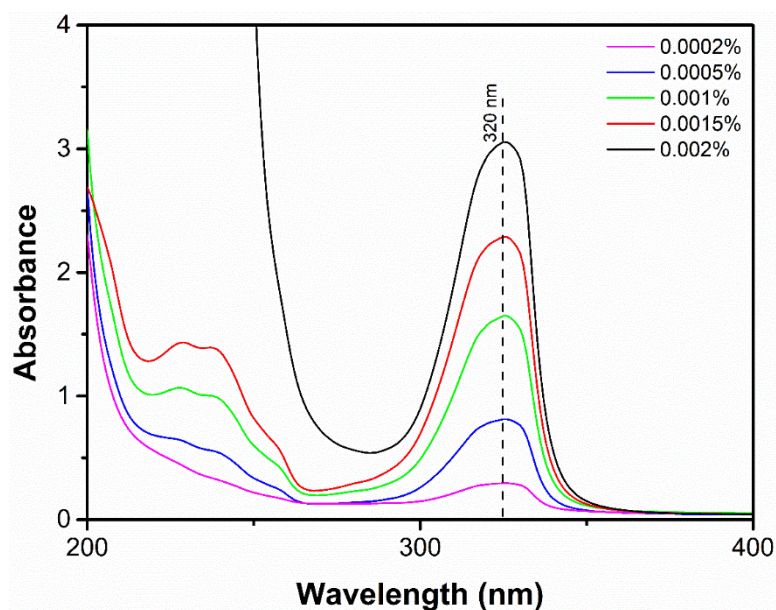


Figure 20: UV-Vis curves for different amount of MBT in ethanol

The absorbance peaks' values for different MBT concentrations are listed in Table 2

Table 2: Absorbance peak values at 320 nm for different MBT concentrations

C [%]	0.002	0.0015	0.001	0.0005	0.0002
A (320 nm)	2.94 ± 0.124	2.21 ± 0.0535	1.57 ± 0.0638	0.78 ± 0.177	0.29 ± 0.0455

From the values in Table 2 it is possible to create a linear regression curve (Figure 21) and to extrapolate an equation that will be used for MBT loading percentage evaluation. It is important that MBT concentrations and their relative absorbance peaks are still in linear region.

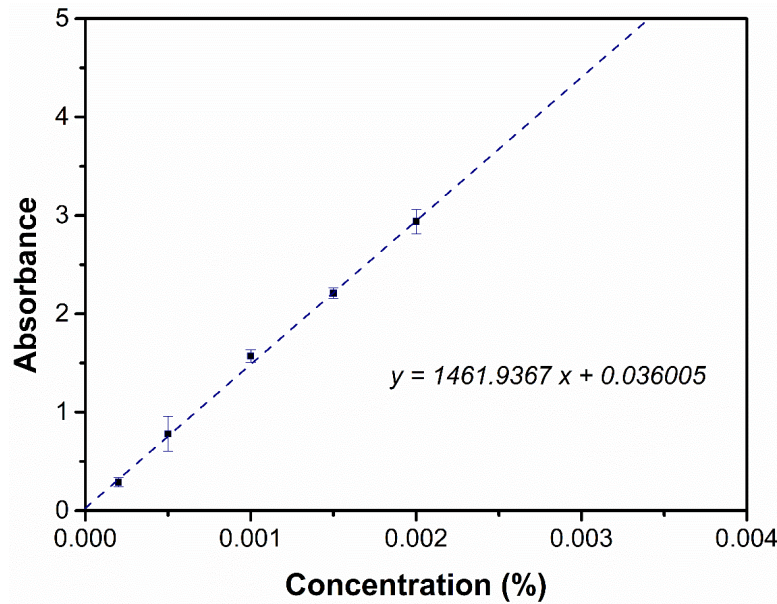


Figure 21: Peak heights at 320 nm for different MBT concentrations, fit plot and linear regression

In order to evaluate the loading efficiency, the amount of MBT successfully loaded need to be evaluated. The absorbance peak is converted into MBT concentration through the above shown equation in Figure 21. Then, the amount of MBT per mL and then per volume of solution is evaluated. In this case the solution was diluted, and thus the amount per 2 mL solution is evaluated. Then, the total volume of solution is divided per volume used in dilution, in this case 0.2 mL (for 2 mL 10 times diluted solution). Multiplying per MBT amount obtained before, the total MBT amount in the total volume of solution is obtained. Through a simple formula

$$\text{Loading efficiency (\%)} = \frac{M_{MBT,l}}{M_{MBT,u}} \times 100 \quad 15)$$

Where $M_{\text{MBT},l}$ is the loaded MBT amount, and $M_{\text{MBT},u}$ is the used MBT amount.

Figure 22 shows the UV-Vis curves of the final nanocomposite. In order to obtain reliable results, with absorbance values in the linear region, the polymer has been diluted 10 (blue) and 100 (red) times.

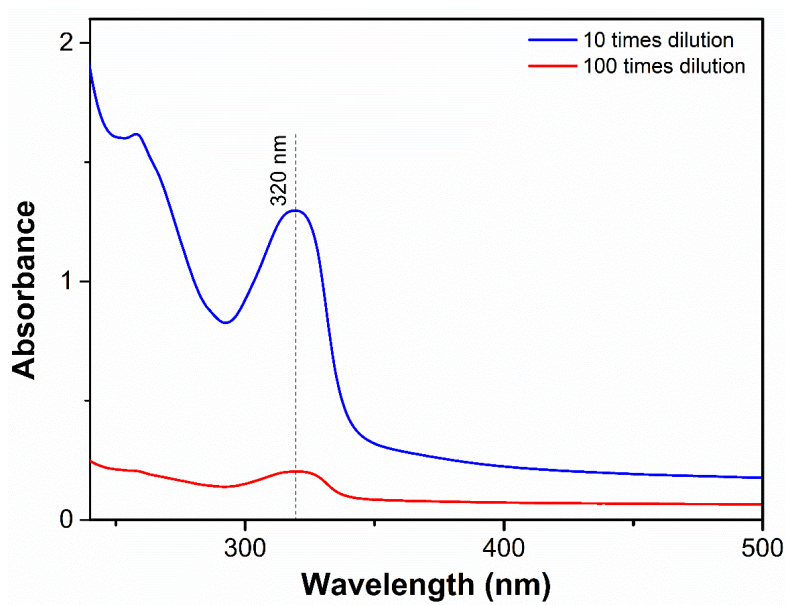


Figure 22: UV-Vis profile of pollen/CS/ZnO polymer, 10 (blue) and 100 (red) times dilution

The observed peaks' heights at 320 nm are shown in Table 3:

Table 3: peaks heights for polymer UV-Vis curves

Dilution	10 times dilution	100 times dilution
Peak height	1.297	0.203

Though the equation expressed in Figure 21 and through Eq. 15, the loading efficiency is calculated to be $55 \pm 7 \%$. The uncertainty is mostly due to the high level of precision required for dilution, and since very small amount are dealt with, small inaccuracies can lead to high uncertainties. Despite the quite high uncertainty related to the measurement, even a 50% of loading efficiency would be considered a good result. A very simple loading method is demonstrated to be suitable to load anticorrosive agent into pollen grains, and a sufficient quantity of MBT has been loaded to guarantee protection from corrosion.

3.3 Pollen

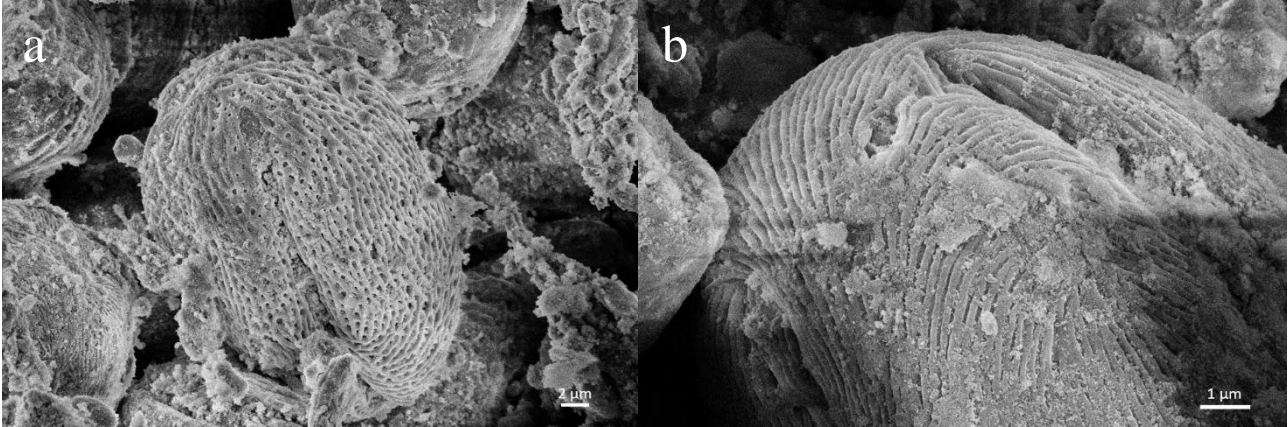


Figure 23: SEM images of treated pollen, with only ethanol (a) and with formaldehyde (b)

Figure 23 shows a pollen grain treated with only ethanol (Figure 23a) and with ethanol and formaldehyde (Figure 23b). As anticipated in the methods section, no clear difference is observable from the comparison of the two images. Pollen grains shape and dimensions, with an average of 20 μm , are the same, and the presence of some dirt on the surface is detectable in both the samples. Figure 23a shows slightly increased porosity when compared to Figure 23b, but this can be related to SEM quality of images and not to the treatment itself. We thus conclude that both treatments can be successfully used to clean the majority of impurities and organic substances to free space for anticorrosion carrier agent. Despite no major differences are encountered when comparing the two samples, pollen treated with ethanol is preferable since the ease of application and time saving when compared to formaldehyde treatment.

The average thickness of pollen grains has been evaluated as 20 μm . Quite large variation of pollen grains' dimensions has been encountered, with grains spacing from 5 to 35 μm .

3.4 Viscosity

Results of dynamic viscosity measurements, each done three times, are shown in Table 4

Table 4: Dynamic viscosity of chitosan-based solutions

Composition	Dynamic viscosity [$\text{mPa} \cdot \text{s}$]	Standard deviation
CS	4.24	0.053
CS-GA 3%	3.63	0.072
CS-GA 7%	5.031	0.042
Composite	3.742	0.02

Despite all the values are lower than expected and lower than the one reported in literature [28], where values of around 30 mPa·s are expected, their behaviour upon addition of GA and pollen/ZnO NPs is as expected. Upon addition of small amount of GA, in fact, chitosan would not form a network but would be partially crosslinked. Chitosan chains are believed to change from coil-like structure [94] to a collapsed one, thus decreasing the dynamic viscosity. With increased amount of GA, chitosan is believed to organize in a network that shows higher values of viscosity. Last, the introduction of large pollen grains and their interaction with chitosan molecules would partially “brake” the network resulting in a further decrease of dynamic viscosity.

3.5 Sample morphology

3.5.1 Optical microscope

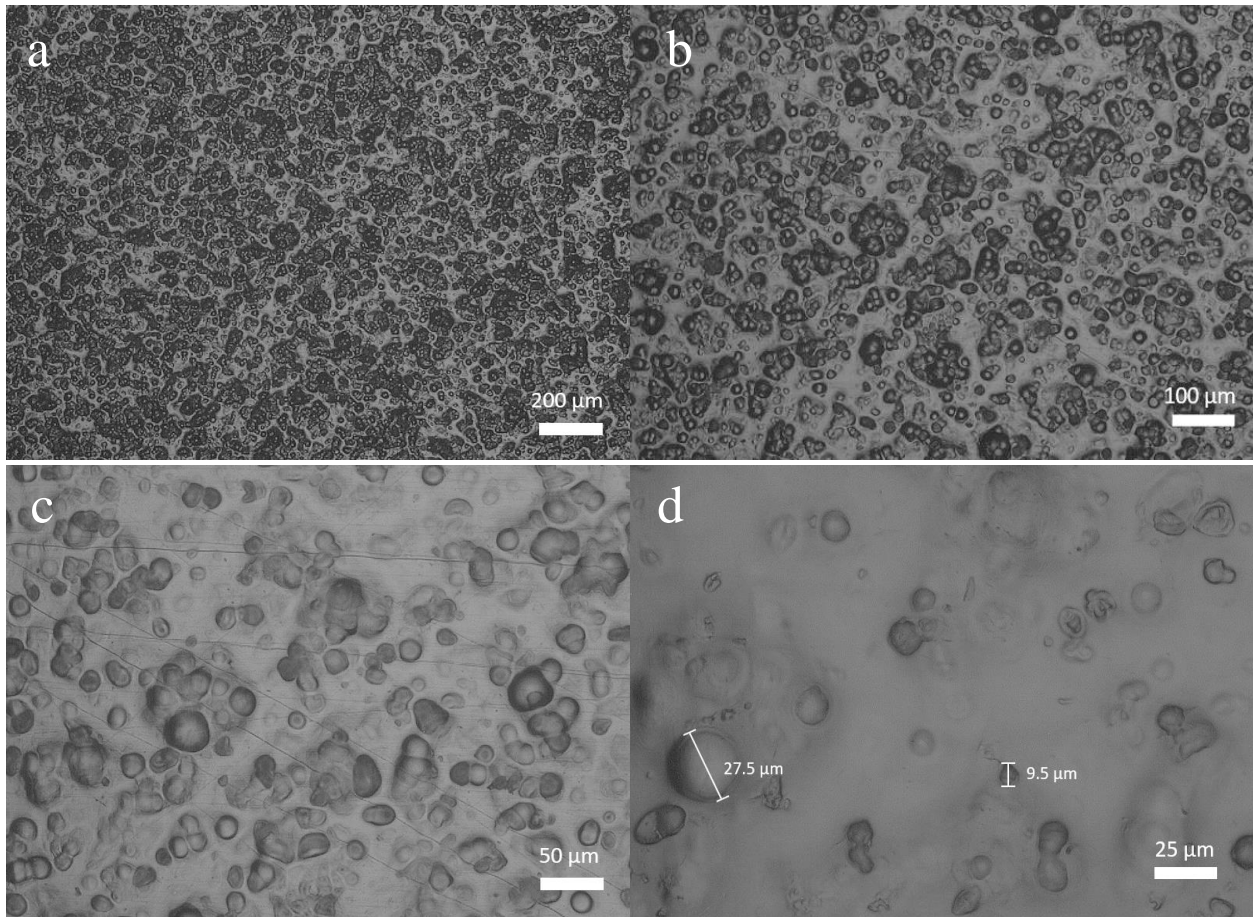


Figure 24: Optical microscope images from lower to higher magnification (a-d)

Figure 24 shows the coating morphology inspected through optical microscope. Figure 24a shows a good homogeneity all over the surface. Despite Figure 24b shows the slight tendency of agglomerating in bigger clusters, this kind of morphology is believed to be good enough for the coating purposes. In Figure 24c a broad dimension distribution is showed for pollen grains, while in

Figure 24d the different dimensions of grains are observed to be ranging from around 9 μm up to almost 30 μm .

An interesting comparison with Figure 25, obtained from a first attempted coating, shows that the final polymer overcame some main defects present at the beginning. In particular, looking at Figure 24d and Figure 25a, the microcracks shown in the latter are not present in the final coating, that looks far more integer with respect to previous attempts. The circle-like defects observable in Figure 25b, attributed to the drying of chitosan around the large pollen grains, are not encountered when observing Figure 24. We can thus conclude that the use of GA 9% used in the last composite helps overcoming some main morphological issues encountered in the first sample. Thus, the origin of these defects, first only theoretically attributed to the viscosity of the polymer, became more clearer and could be finally attributed to the viscosity.

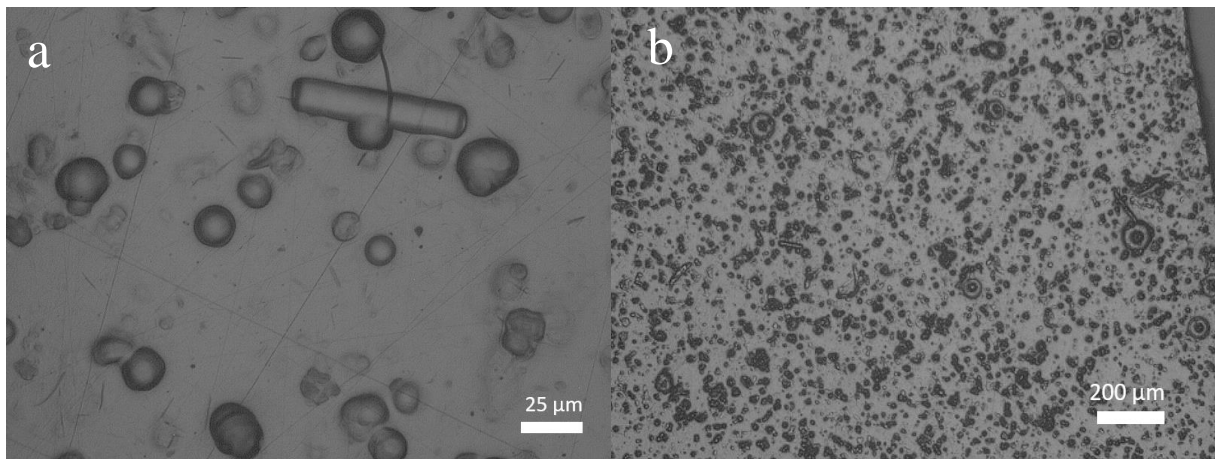


Figure 25: optical microscope images to focus on microcracks (a) and hall defects (b) in failed coating

3.5.2 SEM

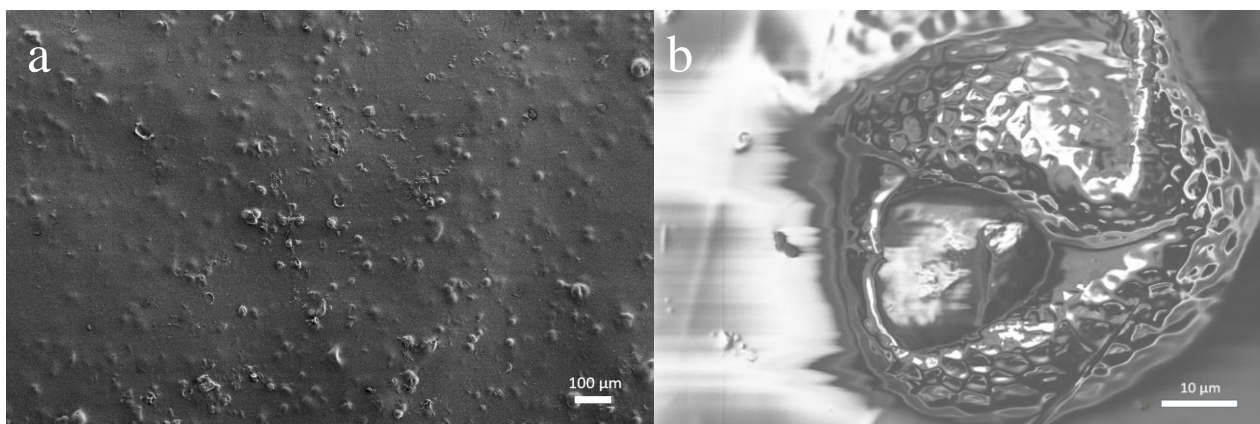


Figure 26: SEM images of coating, low magnification (a) and a detail (b)

Figure 26 shows a low magnification view of the coating (a) and a detail of pollen grain (b). Figure 26a does not give more information about the coating with respect to optical microscope images, apart from a more 3-dimensional view of pollen grain onto the surface. Some minor defects are still visible, as small holes, but in general the integrity of the surface looks good, without major defects that could affect the performances of the coating. Figure 26b shows an interesting detail of pollen grain. Despite the image is similar to the one shown in Figure 23a, it is important to have a view of the pollen grains when embedded in the chitosan matrix, as they will play an important role in passive corrosion resistance.

3.6 Sample performances

3.6.1 Thickness

As mentioned in the methods section, thickness has been evaluated through a thickness gauge with the mean value out of three measurements. Since the dimensions of the pollen grains, a good thickness is considered to be $>50\text{ }\mu\text{m}$.

Different coating compositions' thicknesses are reported in Table 5.

Table 5: Thickness measurements for different coating compositions

Composition	CS-GA3%	Non-top coated	SA top coated	PMAO top coated
Thickness [μm]	34 ± 4.4	49 ± 2.7	52 ± 3.4	53 ± 4.1

3.6.2 Surface attachment

As mentioned in section 2.2.6, numerous tests have been carried out to improve surface attachment of the coating. Surface attachment, as explained in the introduction section, is one of the key parameters to have a performing coating, and much work has been thus focused on this. The lack of primer resulted in an inhomogeneous distribution of particles in the coating, and its cross-section was not analyzed.

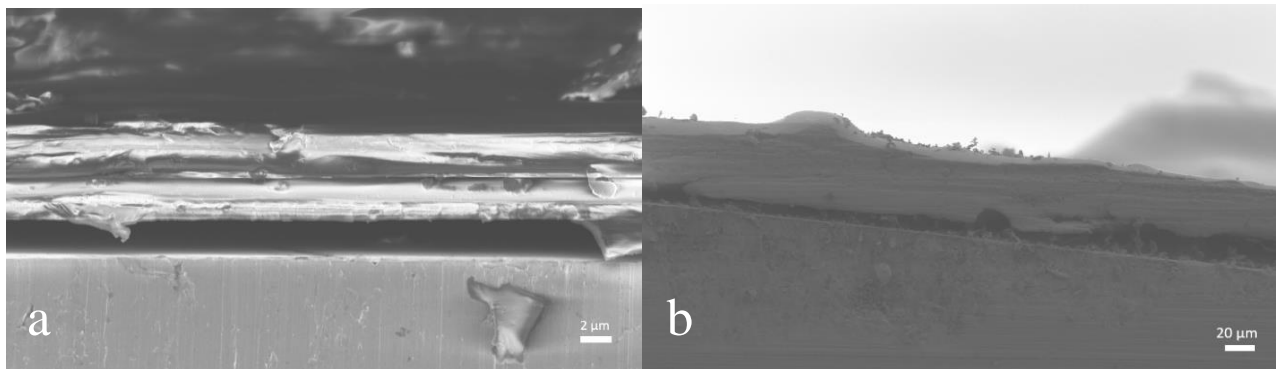


Figure 27: SEM images of tannic acid primer sample (a) and MUA primer sample (b)

Figure 27 shows the cross-section SEM images of tannic acid and MUA primers samples. Despite small improvements seem achievable through the use of MUA, the latter cannot be considered satisfactory as Figure 27b still shows a gap between the coating and the metal substrate. Moreover, when comparing the results with

Figure 28, obtained through spray coating of bare chitosan solution onto MUA primer on metal surface, the difference is clear, as the latter does not show any gap. The first conclusion is that MUA can be successfully used as primer, but probably the large pollen grains influence the attachment of the coating to the metal substrate. Thus, new sample are prepared with a first layer of chitosan solution on the MUA primer, followed by spray coating of the composite. Moreover, the influence of the grinding is analyzed comparing fine grinding and coarse grinding.

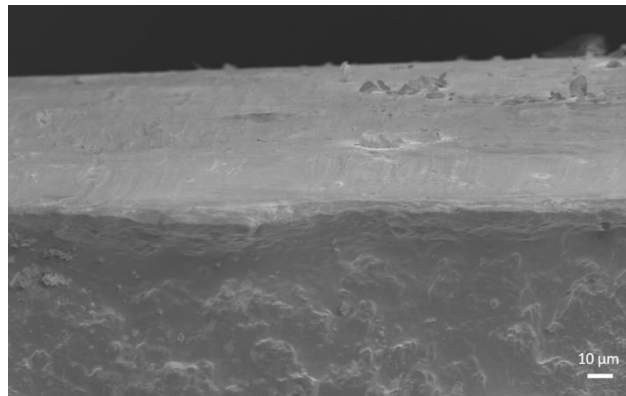


Figure 28: SEM image of MUA primer and chitosan sample

Figure 29 shows a fine grinded metal substrate (a) and a coarse grinded metal substrate (b). both the samples were obtained though MUA primer, chitosan layer followed by spray coating of the polymer. The coarser grinded sample seems to have a better attachment when compared to the finer grinding, and thus coarser grinding is used for the further tests.

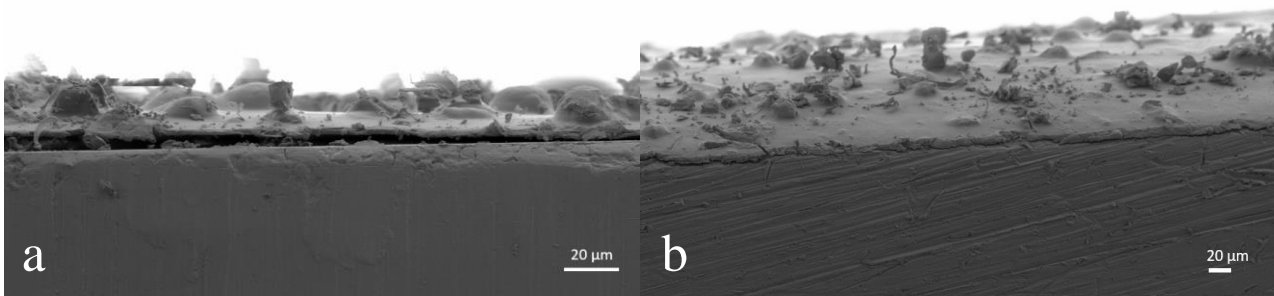


Figure 29: SEM images of fine (a) and coarse (b) grinded surface followed by MUA primer, chitosan layer and coating

Despite Figure 30a shows very good attachment of coating to the metal surface, Figure 30b suggests that the homogeneity of the attachment is not achieved all over the cross-section. This inhomogeneity is not very well explained, and thus the idea that the cross-section preparation, comprehending the grinding and the gold nanoparticles covering for SEM analysis, might influence the quality of the coating when analyze with SEM. Thus, the cross section is inspected though optical microscope (Figure 31)

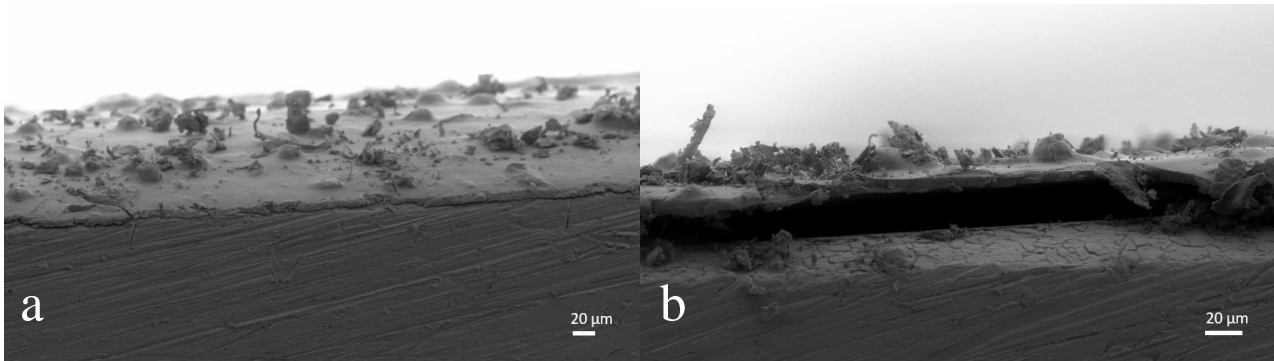


Figure 30: SEM images of MUA primer, chitosan first layer and polymer

Despite the lower quality of the image with respect to SEM images, Figure 31 helps in the analysis of cross-section. It seems clear that the attachment to metal substrate looks very good, with no gap between the coating-metal interface. Moreover, the attachment is homogenous all over the cross-section, and since the coating design is the same of the one showed in Figure 30, we can thus conclude that MUA can be successfully applied as primer and the final attachment of the coating to metal substrate is good.

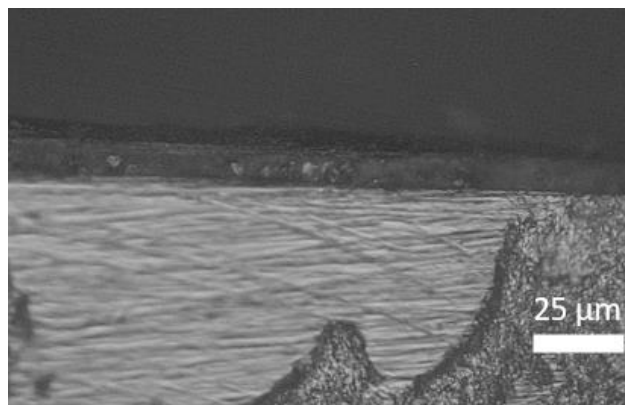


Figure 31: Optical microscope image of MUA primer, chitosan layer and polymer

3.6.3 FT-IR

Figure 32 shows the FT-IR curves of chitosan (red line), crosslinked chitosan with GA 3 wt% with respect to chitosan (blue line) and non-top coated coating (green line).

The 3367 cm^{-1} peak is characteristic of N-H stretching absorption from primary amine (NH_2) of chitosan chain, while the peak at 3235 cm^{-1} is attributed to OH stretching. The CH stretching for the peaks at 2920 and 2871 cm^{-1} are referred to symmetric and asymmetric stretching, respectively [95]. The peak at 1648 cm^{-1} is probably related to residual N-acetyl groups, in this case C=O for amide I, while the peak at 1334 cm^{-1} is probably related to C-N stretching for amide III [95]. The peak at 1547 cm^{-1} can be attributed to N-H of amide II, but the N-H peak for amide I ($1580\text{--}1650\text{ cm}^{-1}$) is not found. CH_2 and CH_3 peaks might be overlapped in the peak at 1400 cm^{-1} . The peaks at 1066 and 1015 cm^{-1} can be attributed to C-O stretching bond. Last, peak at 1148 cm^{-1} is characteristic of C-O-C bridge. To conclude, the presence of chitosan is confirmed by the FT-IR analysis.

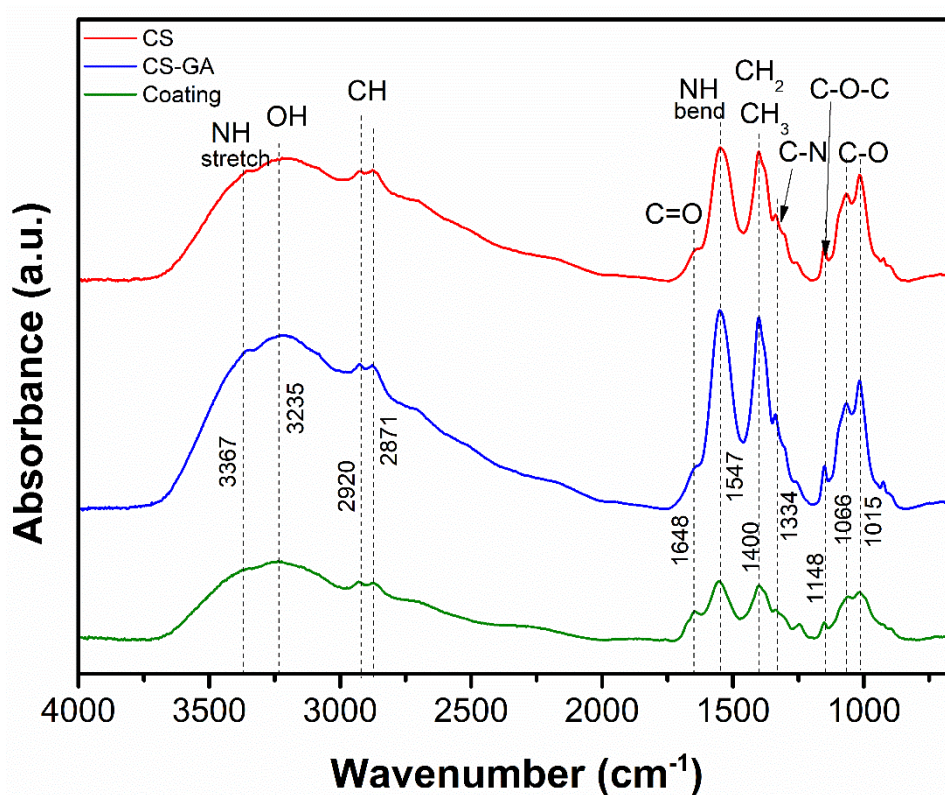


Figure 32: FT-IR curves of non-crosslinked chitosan, crosslinked chitosan and coating

What differs from the different spectra is the ratio between some peaks. Particularly important is the comparison between crosslinked and non-crosslinked chitosan (blue and red curves, respectively) and the comparison between crosslinked chitosan and final coating (blue and green, respectively).

As per the reaction mechanism described in section 2.2.3, glutaraldehyde is supposed to react with primary amino groups of chitosan to form imine group. Thus, the effect on FT-IR spectra should be the decrease of the ratio between the peak relative to N-H bending of primary amine (NH_2) and the peak relative to C=O of amide group. Unfortunately, the N-H bending of primary amine has not been found in the FT-IR spectra, and the carbonyl stretching vibration peak is not increased consistently

despite the amine bond peak should superimpose. From the comparison of the two curves, it seems that the peaks at 1547 cm^{-1} and 1400 cm^{-1} , relative to NH bend and CH_2 and CH_3 , slightly increase in the ratio with the other peaks group, from 3367 cm^{-1} to 2871 cm^{-1} and from 1148 cm^{-1} to 1015 cm^{-1} . The increase of 1547 cm^{-1} might be due to superimposition of ethylenic bond peak due to a contribution of glutaraldehyde in the chitosan-glutaraldehyde reaction to increase the crosslinking chain [78].

When analysing the FT-IR curves characteristic of the coating, the main changes with respect to chitosan-GA can be summarized as the decrease of the ratio relative to C-O stretching bond (1066 and 1015 cm^{-1}), the increase of C=O peak at 1648 cm^{-1} and an decrease of the ratio of the 1547 cm^{-1} to 1334 cm^{-1} group and the 3367 cm^{-1} to 2871 cm^{-1} and 1148 cm^{-1} to 1015 cm^{-1} groups. The increase of C=O peak can be attributed to PMAO chains, while the changes observed for the C-O peaks at 1066 and 1015 cm^{-1} can be due to C-O bonds from PMAO molecules' not-opened rings.

3.6.4 Water contact angle

Several contact angle measurements have been done on different samples: non top coated sample, obtained with pollen/CS/ZnO composite and GA 9%, top coated with PMAO solution and top coated with SA solution, since they represent the most interesting study-cases encountered. Contact angle measurements are listed in Table 6

Table 6: Contact angle of different compositions samples

Composition	<i>Non- top coated</i>	<i>PMAO top coated</i>	<i>SA top coated</i>
Contact angle	$25.75 \pm 0.84^\circ$	$112.85 \pm 0.26^\circ$	$134.32 \pm 3.84^\circ$

Figure 33a and values in Table 6 show a very low contact angle for non-top coated sample, with respect to 40° contact angle from literature. One possible explanation is that highly porous pollen grains on the surface absorb water, thus decreasing the hydrophobicity of the coating. The use of top coating seems thus necessary to ensure hydrophobic behaviour.

As it can be seen, a more hydrophobic behaviour is shown by the SA top coated sample. Despite a good increase in contact angle seems to be achievable with PMAO top coat, results are far more negative when compared to SA top coat and to literature [22]. From a water contact angle measurement point of view, SA topcoat thus seems the best option to improve hydrophobicity of the sample to withstand the water environment the coating is thought to work in. Nevertheless, the absence of prints left by the water drop on PMAO top coated sample is a promising aspect.

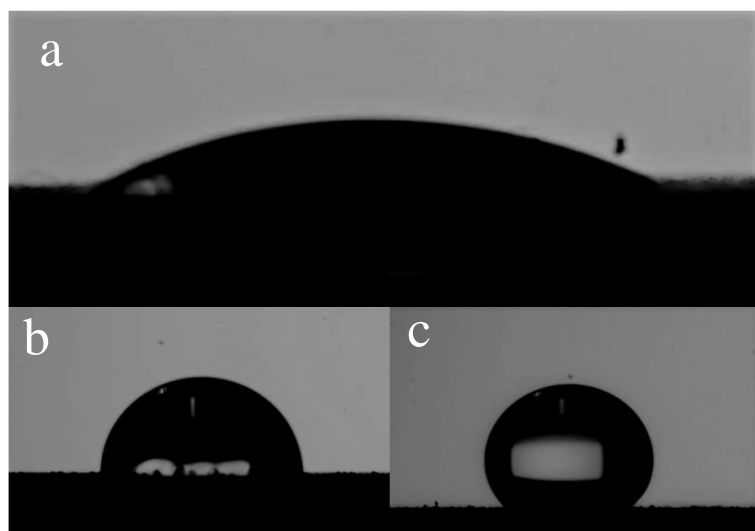


Figure 33: Contact angle image of non-top coated sample (a), PMAO top coated sample (b) and stearic acid top coated sample (c)

3.6.5 Anticorrosion behavior

Figure 34 shows the EIS plots of PMAO top coated sample. This sample has been considered since it clearly shows a transformation in behavior over time. The two plots in Figure 34, in fact, show the measurements at five different times, t1, t2, t3, t4 and t5. Each test was separated by an OCP measurement 2 h long, in order to allow the system to reach the equilibrium potential. Figure 34a shows the Nyquist plot of EIS measurement and the magnified representation of the low Z' and Z'' region. Figure 34b shows the Bode plot of EIS measurement, phase vs. frequency. A magnified representation of high frequency range is also given for Figure 34b.

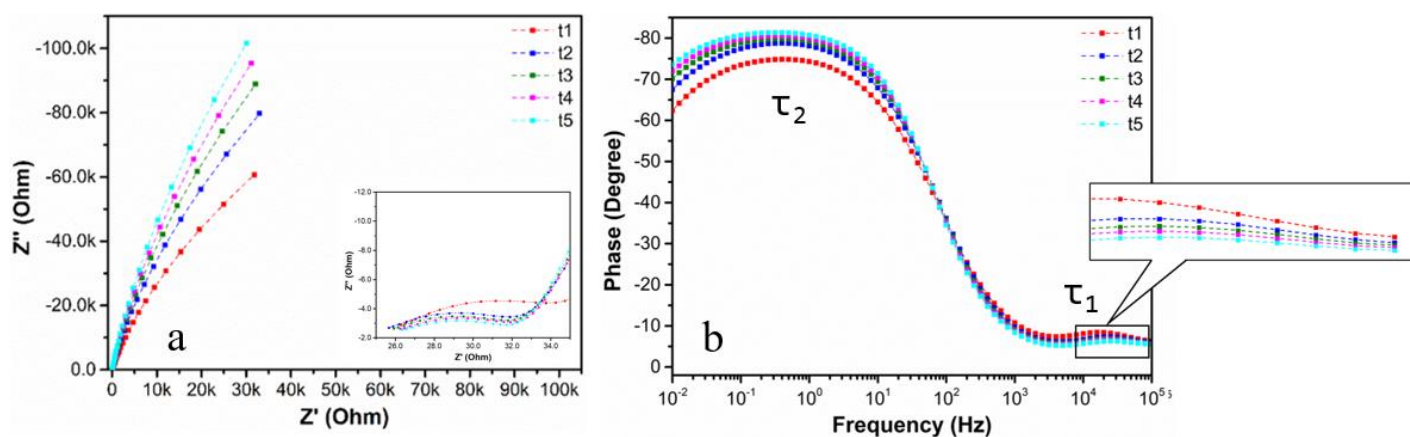


Figure 34: EIS plot of PMAO top coated sample. Nyquist plot (a) and Bode plot, phase vs. frequency (b)

Figure 34a shows better corrosion resistance given by the last measured coating since the semicircle is wider than the one obtained for t1 measurement, thus suggesting higher polarization resistance. When analyzing the magnified image, the typical failed coating shape is observed, with two semicircles. If this is the case, very low values of impedance are detected for the first semicircle,

relative to pore/coating resistance (Figure 7 in the introduction section). The large second semicircle would be characteristic of the oxide layer of stainless steel when in contact with the electrolyte that accumulated on its surface after penetrating the coating. Figure 34b is in agreement with the above explanation. High frequencies region (magnified image), in fact, usually represents the coating-electrolyte interface. With increasing time, the resistance decreases (t_1 to t_5 curves). This can be explained by the fact that always more water penetrates the coating, thus decreasing its resistance. At low frequencies usually the metal-coating interface is represented. Here, resistance increases with increasing time. A possible explanation is that at the metal-coating interface water is accumulating, reacting with stainless steel and increasing the natural oxide layer, and thus the corrosion resistance. Looking at Figure 34a, since the resistance is increasing with time, it seems that the protection given by the growing oxide layer is more effective than the coating resistance itself.

Figure 35 shows the suggested equivalent circuit for PMAO top coated sample.

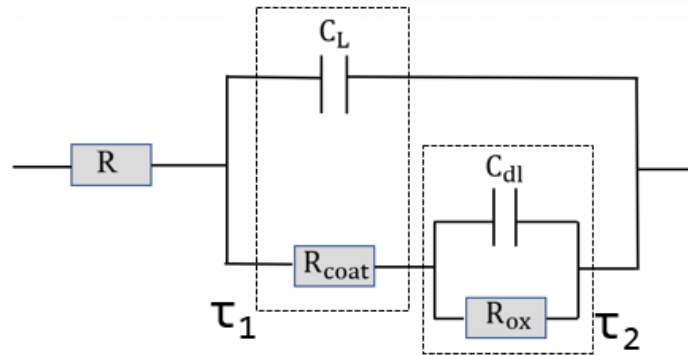


Figure 35: Equivalent circuit for PMAO top coated sample

τ_1 and τ_2 represent the two time constants individuated in Figure 34b. As anticipated, the high frequencies ($10^3 - 10^5$ Hz range) time constant, τ_1 , represents the electrolyte-coating interface, suggesting a resistance characteristic of the coating. At low frequencies only one time constant is individuated, τ_2 , and it has been associated with the resistance proper of the protective oxide layer that is formed on stainless steel. To conclude, the PMAO top coated sample shows the typical coating resistance at high frequencies and the oxide resistance at low frequencies. No charge transfer resistance is detected, thus suggesting that corrosion is delayed by the coating and the oxide layer.

Figure 36 shows the EIS measurement plots for 5 different surfaces: bare stainless steel (blue line), chitosan-GA 3 wt% (red line), non- top coated coating (magenta line), stearic acid top coated sample (green line) and PMAO top coated sample (cyan line). Figure 36a shows the Nyquist plot with a magnified representation of low impedance values while Figure 36b shows the Bode plot of EIS measurements, phase vs. frequency.

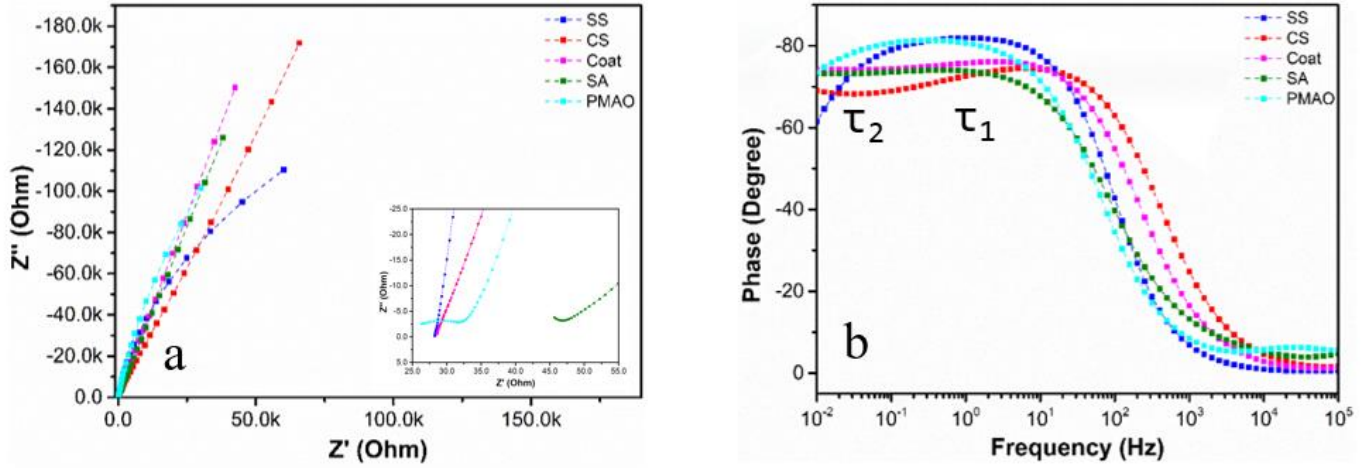


Figure 36: EIS plot of different coated samples. Nyquist plot (a) and Bode plot, phase vs. frequency (b)

Figure 36a shows, for SA and PMAO top coated samples, a similar behaviour with respect to the one represented in Figure 34a. Both the samples show failed coating behavior, despite the SA top coated has slightly higher impedance values than PMAO top coated sample. Chitosan and non-top coated sample (called “coat”, magenta line) do not show any double semicircle behavior. We can conclude that their coating resistance is that low that it is not even detected, and they just represent a stainless steel in contact with electrolyte behavior. Figure 36b confirms the above analysis. It shows that at high frequencies a better resistance is given by SA and PMAO top coated samples, while at low frequencies the non-top coated resistance is similar to the top coated ones. Despite the coating contribution looks almost null, Figure 36a shows that, for all coated samples, the resistance is increased with respect to bare stainless steel sample. Despite all coating, at a certain point, are penetrated by water, somehow they might show a slight positive influence on resistance. As it was done for PMAO top coated sample, also in Figure 36b two time constants have been individuated, τ_1 and τ_2 , both at low frequencies.

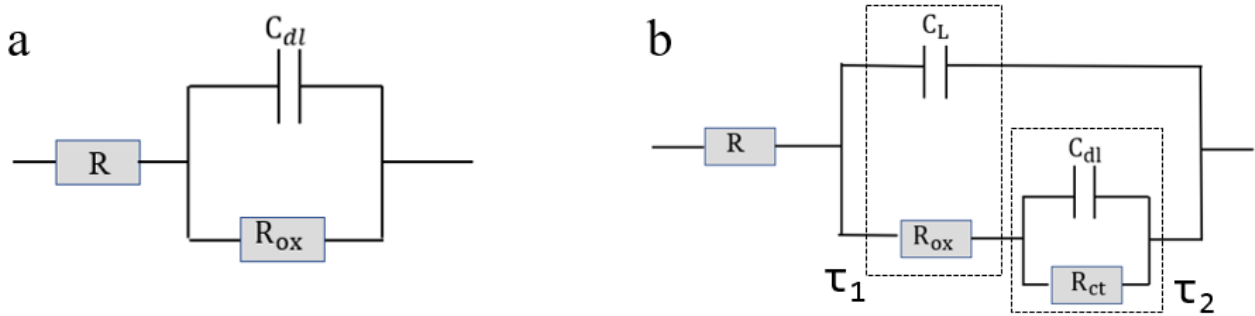


Figure 37: Equivalent circuits for different coatings

Figure 37 shows the two equivalent circuits used to explain the behavior of the coatings. Figure 37a shows the equivalent circuit associated with the curves proper of stainless steel and SA top coated sample. Only one constant is in fact observed in Figure 36b when analyzing the two curves. A possible

explanation is that the coating is not detected (no time constant at high frequencies), but the oxide layers delay the diffusion of ions enough not to detect any charge transfer reaction resistance. The resistance observed is thus proper of the oxide layer. Both chitosan coating and composite coating show two time constants at low frequency, τ_1 and τ_2 shown in Figure 36b, and no time constant for the coating. A possible explanation is that the barrier action is so poor that is not even detected, and the two constants can be associated with the oxide layer resistance (τ_1) and charge transfer resistance (τ_2). The oxide layer lets the ions pass and reach the metal surface, where a charge- transfer reaction occurs. The chitosan and non-top coated samples can be thus represented by the equivalent circuit shown in Figure 37b.

The equivalent circuit analysis shows that only PMAO top coated sample has the coating characteristic behavior. Despite the small improvements in corrosion resistance shown in Figure 36a, the too small coating resistance of PMAO and partly of SA top coated samples is not encouraging and most likely underline that these coating are not suitable for full immersion conditions if the bulk properties of the composite are not enhanced. The increase of hydrophobicity, though both PMAO and SA, led to some encouraging improvements with respect to the other coatings, represented by coating resistance for PMAO (Figure 34a). and the retarding of ion diffusion (since the lack of charge transfer resistance) for SA. These two coatings can be thus used for alternating immersion or atmospheric corrosion protection, mostly when combined to an already corrosion resistant metal as stainless steel.

4 CONCLUSIONS

Chitosan nanocomposite composed of chitosan matrix loaded with ZnO nanoparticles and bee pollen as carrier for anticorrosion agent MBT has been successfully prepared. The treated chitosan has 93.3 ± 0.48 % of degree of deacetylation. The result of quantification of 2-mercaptobenzothiazole shows a successful loading of anticorrosive agent into pollen grains. A phase transfer method employing PMAO enables the stable aqueous suspension of pollen and further carbodiimide crosslinking with chitosan ensure their dispersion in chitosan matrix.

Several attempts were carried out and a successful coating application method has been realized. Despite multiple coating steps must be applied to reach a satisfactory thickness of around 50 μm , spray coating resulted in a homogeneous coating and easy application method, thus being reliable for larger scale production. The surface pretreatment, moreover, suggested a higher bonding of the coating when a coarser grinding is applied to the metal surface. This is due to mechanical bonding due to the “teeth” of the metal surface. Two different primers, 11-mercaptopundecanoic acid and tannic acid, have been proved to be possible primers for the coating. The coating itself, before being applied onto the primer, is believed to get beneficial effect if first a 15 μm layer of bare chitosan solution is applied onto the primer. This is due to pollen grains that, having an average dimension of 20 μm , might influence the strength of bonding of the coating.

Pollen grains themselves are believed to have a bad influence on the water resistance of the coating. Optical microscope images show microcracks that might be due to the drying of chitosan around the large pollen grains. Pollen grains are also believed to absorb water, thus showing more hydrophilic behavior of the coating when compared to bare chitosan coating. To this end, a stearic acid and a PMAO topcoats are successfully applied to highly increase the contact angle from $25.75 \pm 0.84^\circ$ to $134.32 \pm 3.84^\circ$ and $112.85 \pm 0.26^\circ$, respectively. This large increase of hydrophobic behaviour is believed to have beneficial effect on anticorrosion properties of the coating.

FT-IR curves show the expected peaks for chitosan, in accordance with literature. GA addition, despite a few controversial changes in the peaks' intensity, can be seen in the FT-IR curves when compared to non-crosslinked chitosan. The FT-IR spectra of composite-coated sample shows the effect of molecules addition, mostly PMAO, that results in decrease of the ratio relative to C-O stretching bond (1066 and 1015 cm^{-1}), the increase of C=O peak at 1648 cm^{-1} and an increase of the ratio of the 3367 cm^{-1} to 2871 cm^{-1} group and the 1547 cm^{-1} to 1334 cm^{-1} group.

EIS measurements show that, despite the increase of hydrophobicity due to SA and PMAO top coating, coating corrosion resistance is very low. In particular, SA top coated sample does not even show any coating resistance, and its positive effect on corrosion resistance is given by retarding the ion diffusion to the metal surface. PMAO, on the contrary, shows the typical behaviour of coating, but the coating resistance module is too low to be considered as a possible solution for full immersion conditions. Since small improvements are obtained through the use of coating, the latter could be used as atmospheric corrosion resistance coating.

To conclude, despite several characterization steps are still missing to obtain a fully working coating with all the desired features mentioned in the introduction section, the first steps in the development of a 100% natural coating for corrosion protection have been done. Efforts is needed in future to

improve this technology and to further develop it to a complete anticorrosion, self-healing and anti-biofouling coating.

5 FUTURE WORK

Future improvements on coating properties and anti-corrosive performance are planned. First, the water uptake needs to be minimized. Despite the use of stearic acid led to improvements in this sense, water still penetrates the coating after some time, thus making it not suitable for long-period anticorrosion application. Further studies on the passive protection through MBT must also be carried out. The first EIS results suggest an active protection behavior through the barrier action of the coating, but the passive corrosion resistance due to MBT loading into pollen needs to be tested. Together with MBT release and protection effectiveness, self-healing properties need to be studied. To this end, as suggested in the method section, EIS can be used to seek for any changes in polarization and impedance after scratching the surface. An increase of impedance would suggest a protection action due to MBT or chitosan self-healing. Unfortunately, the creation of oxide layer typical of stainless steel could influence the reading of the EIS after scratching. To this end, the application of the coating to other surfaces, such as carbon steel, aluminum, and copper, need to be considered in order to extend the application scenario.

At last, the antimicrobial activity needs to be tested as well. Despite from literature that the beneficial effect of chitosan and ZnO NPs on bacterial removal has already been proved, it will be interesting to investigate antimicrobial effects of the developed formulations.

6 ACKNOWLEDGMENTS

I wish to extend my deepest gratitude to Prof. Joydeep Dutta, who believed in me and in this master's project. His passion and enthusiasm guided me towards these months. Thank you for letting me grow and for being so direct with your students, with whom you are always able to connect and inspire. Thank you, Dr. Fei Ye, you followed me step by step and bridged my chemistry gaps with patience. Thanks to Dr. Abdusalam Uheida who managed my spaces and ensured my safety in the chemistry lab, who was always available for interesting and broad discussions. Thanks to Prof. Pavel Korzhavy, for supporting me and helping me to finalize this report.

All my gratitude to all the FNM group, that created a perfect environment to work with joy and enthusiasm. Special thanks to Esteban Toledo and Maria Isabel for sharing your knowledge with me and for bearing my non-always positive attitude. We had lot of fun and I would like to thank you for this.

I would also like to express my gratitude to all the Materials Science Department in KTH for welcoming me in this exciting master experience and for helping me grow both professionally and personally.

7 REFERENCES

1. Roberge, P.R., *Handbook of corrosion engineering*. 2000, New York: New York : McGraw-Hill.
2. *Terminology Relating to Corrosion and Corrosion Testing*. ASTM International.
3. Petrovic, Z., *Catastrophes caused by corrosion*. Vojnotehnicki glasnik, 2016. **64**(4): p. 1048-1064.
4. Koch, G., *1 - Cost of corrosion*, in *Trends in Oil and Gas Corrosion Research and Technologies*, A.M. El-Sherik, Editor. 2017, Woodhead Publishing: Boston. p. 3-30.
5. Koch, G.H., et al., *Chapter 1 - Cost of corrosion in the United States*, in *Handbook of Environmental Degradation of Materials*, M. Kutz, Editor. 2005, William Andrew Publishing: Norwich, NY. p. 3-24.
6. Fontana, M.G., *Corrosion engineering*. 2. ed.. ed, ed. N.D. Greene. 1978, New York: New York.
7. Cicek, V., *Corrosion Engineering and Cathodic Protection Handbook - With Extensive Question and Answer Section*. John Wiley & Sons.
8. Roberge, P.R., *Corrosion engineering: principles and practice*. 2008, New York: New York: McGraw-Hill.
9. Sørensen, P.A., et al., *Anticorrosive coatings: a review*. Journal of Coatings Technology and Research, 2009. **6**(2): p. 135-176.
10. *Corrosion and Protection*. 2004, London: Springer London, London.
11. Uhlig, H.H. and C.V. King, *Corrosion and Corrosion Control*. Journal of The Electrochemical Society, 1972. **119**(12): p. 327C.
12. Taylor, S.R., *Coatings for Corrosion Protection: Organic*, in *Encyclopedia of Materials: Science and Technology*. 2001, Elsevier. p. 1274-1279.
13. Steinsmo, U. and E. Bardal, *Factors Limiting the Cathodic Current on Painted Steel*. J. Electrochem. Soc, 1989. **136**(12): p. 3588-3594.
14. Tofa, T.S., et al., *Enhanced Visible Light Photodegradation of Microplastic Fragments with Plasmonic Platinum/Zinc Oxide Nanorod Photocatalysts*. Catalysts, 2019. **9**(10): p. 819.
15. Talvitie, J., et al., *Do wastewater treatment plants act as a potential point source of microplastics? Preliminary study in the coastal Gulf of Finland, Baltic Sea*. Water Science and Technology, 2015. **72**(9): p. 1495-1504.
16. Shim, W.J., S.H. Hong, and S. Eo, *Marine Microplastics: Abundance, Distribution, and Composition*, in *Microplastic Contamination in Aquatic Environments*. 2018, Elsevier. p. 1-26.
17. Talvitie, J., et al., *Solutions to microplastic pollution – Removal of microplastics from wastewater effluent with advanced wastewater treatment technologies*. Water Research, 2017. **123**: p. 401-407.
18. Klein, S., et al., *Analysis, Occurrence, and Degradation of Microplastics in the Aqueous Environment*, in *Freshwater Microplastics : Emerging Environmental Contaminants?*, M. Wagner and S. Lambert, Editors. 2018, Springer International Publishing: Cham. p. 51-67.
19. Tofa, T.S., et al., *Visible light photocatalytic degradation of microplastic residues with zinc oxide nanorods*. Environmental Chemistry Letters, 2019. **17**(3): p. 1341-1346.
20. Lambert, S. and M. Wagner, *Microplastics Are Contaminants of Emerging Concern in Freshwater Environments: An Overview*, in *Freshwater Microplastics : Emerging Environmental Contaminants?*, M. Wagner and S. Lambert, Editors. 2018, Springer International Publishing: Cham. p. 1-23.

21. Shamsheera, K.O., et al., *Stearic acid grafted chitosan/epoxy blend surface coating for prolonged protection of mild steel in saline environment*. Journal of Adhesion Science and Technology, 2019. **33**(20): p. 2250-2264.
22. Carneiro, J., et al., *Functionalized chitosan-based coatings for active corrosion protection*. Surface and Coatings Technology, 2013. **226**: p. 51-59.
23. Carneiro, J., et al., *Chitosan as a Smart Coating for Controlled Release of Corrosion Inhibitor 2-Mercaptobenzothiazole*. ECS Electrochemistry Letters, 2013. **2**(6): p. C19-C22.
24. Ding, F., et al., *Recent advances in chitosan-based self-healing materials*. Research on Chemical Intermediates, 2018. **44**(8): p. 4827-4840.
25. Grundmeier, G., W. Schmidt, and M. Stratmann, *Corrosion protection by organic coatings: electrochemical mechanism and novel methods of investigation*. Electrochimica Acta, 2000. **45**(15-16): p. 2515-2533.
26. *Basics of Electrochemical Impedance Spectroscopy*. 2016; Available from: <https://www.gamry.com/application-notes/EIS/basics-of-electrochemical-impedance-spectroscopy/>.
27. *EIS of Organic Coatings and Paints*. Available from: <https://www.gamry.com/application-notes/EIS/eis-of-organic-coatings-and-paints/>.
28. No, H.K., et al., *Effective Deacetylation of Chitin under Conditions of 15 psi/121 °C*. Journal of Agricultural and Food Chemistry, 2000. **48**(6): p. 2625-2627.
29. Ravi Kumar, M.N.V., *A review of chitin and chitosan applications*. Reactive and Functional Polymers, 2000. **46**(1): p. 1-27.
30. Kim, K.W., et al., *Antimicrobial activity against foodborne pathogens of chitosan biopolymer films of different molecular weights*. LWT - Food Science and Technology, 2011. **44**(2): p. 565-569.
31. Roberts, G.A.F., *Chitin Chemistry*. 1992, Macmillan Education UK.
32. Ali, I., *The Quest for Active Carbon Adsorbent Substitutes: Inexpensive Adsorbents for Toxic Metal Ions Removal from Wastewater*. Separation & Purification Reviews, 2010. **39**(3-4): p. 95-171.
33. ; Available from: https://commons.wikimedia.org/wiki/File:Chitosan_Synthese.svg.
34. Alishahi, A. and M. Aïder, *Applications of Chitosan in the Seafood Industry and Aquaculture: A Review*. Food and Bioprocess Technology, 2011. **5**(3): p. 817-830.
35. Kim, S. and N. Rajapakse, *Enzymatic production and biological activities of chitosan oligosaccharides (COS): A review*. Carbohydrate Polymers, 2005. **62**(4): p. 357-368.
36. Wahba, M.I., *Enhancement of the mechanical properties of chitosan*. Journal of Biomaterials Science, Polymer Edition, 2020. **31**(3): p. 350-375.
37. Njoku, D.I., et al., *Understanding the anticorrosive protective mechanisms of modified epoxy coatings with improved barrier, active and self-healing functionalities: EIS and spectroscopic techniques*. Scientific Reports, 2017. **7**(1).
38. Chakma, P. and D. Konkolewicz, *Dynamic Covalent Bonds in Polymeric Materials*. Angewandte Chemie International Edition, 2019. **58**(29): p. 9682-9695.
39. Al-Naamani, L., S. Dobretsov, and J. Dutta, *Chitosan-zinc oxide nanoparticle composite coating for active food packaging applications*. Innovative Food Science & Emerging Technologies, 2016. **38**: p. 231-237.
40. Dutta, P.K., et al., *Perspectives for chitosan based antimicrobial films in food applications*. Food Chemistry, 2009. **114**(4): p. 1173-1182.
41. Sargin, İ. and G. Arslan, *Chitosan/sporopollenin microcapsules: Preparation, characterisation and application in heavy metal removal*. International Journal of Biological Macromolecules, 2015. **75**: p. 230-238.

42. Kashyap, P.L., X. Xiang, and P. Heiden, *Chitosan nanoparticle based delivery systems for sustainable agriculture*. International Journal of Biological Macromolecules, 2015. **77**: p. 36-51.
43. Zhao, D., et al., *Biomedical Applications of Chitosan and Its Derivative Nanoparticles*. Polymers, 2018. **10**(4): p. 462.
44. Prateepchanachai, S., et al., *Mechanical properties improvement of chitosan films via the use of plasticizer, charge modifying agent and film solution homogenization*. Carbohydrate Polymers, 2017. **174**: p. 253-261.
45. Al-Naamani, L., et al., *Chitosan-zinc oxide nanocomposite coatings for the prevention of marine biofouling*. Chemosphere, 2017. **168**: p. 408-417.
46. Xia, Y., et al., *Biotemplated fabrication of hierarchically porous NiO/C composite from lotus pollen grains for lithium-ion batteries*. Journal of Materials Chemistry, 2012. **22**(18): p. 9209.
47. Kim, S.S. and C.J. Douglas, *Sporopollenin monomer biosynthesis in arabidopsis*. Journal of Plant Biology, 2013. **56**(1): p. 1-6.
48. Li, F.-S., et al., *The molecular structure of plant sporopollenin*. 2018, Cold Spring Harbor Laboratory.
49. Hamad, S.A., et al., *Encapsulation of living cells into sporopollenin microcapsules*. Journal of Materials Chemistry, 2011. **21**(44): p. 18018.
50. Cao, F. and D.-X. Li, *Morphology-controlled synthesis of SiO₂ hollow microspheres using pollen grain as a biotemplate*. Biomedical Materials, 2009. **4**(2): p. 025009.
51. 2008; Available from: <https://en.wikipedia.org/wiki/Pollen#/media/File:RedbudPollen.TIF>.
52. Engels, H.-W., et al., *Rubber, 4. Chemicals and Additives*, in *Ullmann's Encyclopedia of Industrial Chemistry*. 2004, Wiley-VCH Verlag GmbH & Co. KGaA.
53. Rahimi, A. and S. Amir, *Self-healing anticorrosion coating containing 2-mercaptobenzothiazole and 2-mercaptobenzimidazole nanocapsules*. Journal of Polymer Research, 2016. **23**(4).
54. Galvão, T.L.P., et al., *A computational UV–Vis spectroscopic study of the chemical speciation of 2-mercaptobenzothiazole corrosion inhibitor in aqueous solution*. Theoretical Chemistry Accounts, 2016. **135**(3).
55. Feng, Y., et al., *Characterization of iron surface modified by 2-mercaptobenzothiazole self-assembled monolayers*. Applied Surface Science, 2006. **253**(5): p. 2812-2819.
56. Bao, Q., D. Zhang, and Y. Wan, *2-Mercaptobenzothiazole doped chitosan/11-alkanethiolate acid composite coating: Dual function for copper protection*. Applied Surface Science, 2011. **257**(24): p. 10529-10534.
57. Kim, S.-K., *Springer Handbook of Marine Biotechnology*. 1.. ed. 2015: Berlin, Heidelberg : Springer Berlin Heidelberg : Imprint: Springer.
58. Yang, W.J., et al., *Polymer brush coatings for combating marine biofouling*. Progress in Polymer Science, 2014. **39**(5): p. 1017-1042.
59. Flemming, H.-C., et al., *Marine and Industrial Biofouling*. 1st ed. 2009.. ed. 2009: Berlin, Heidelberg : Springer Berlin Heidelberg : Imprint: Springer.
60. Turner, A., *Marine pollution from antifouling paint particles*. Marine Pollution Bulletin, 2010. **60**(2): p. 159-171.
61. Krishnan, S., C.J. Weinman, and C.K. Ober, *Advances in polymers for anti-biofouling surfaces*. Journal of Materials Chemistry, 2008. **18**(29): p. 3405-3413.
62. Lejars, M., A. Margailan, and C. Bressy, *Fouling Release Coatings: A Nontoxic Alternative to Biocidal Antifouling Coatings*. Chem. Rev., 2012. **112**(8): p. 4347-4390.
63. Jennings, M.C., K.P.C. Minbiole, and W.M. Wuest, *Quaternary Ammonium Compounds: An Antimicrobial Mainstay and Platform for Innovation to Address Bacterial Resistance*. ACS Infectious Diseases, 2015. **1**(7): p. 288-303.

64. Yebra, D.M., S. Kiil, and K. Dam-Johansen, *Antifouling technology—past, present and future steps towards efficient and environmentally friendly antifouling coatings*. Progress in Organic Coatings, 2004. **50**(2): p. 75-104.
65. Malini, M., et al., *A versatile chitosan/ZnO nanocomposite with enhanced antimicrobial properties*. International Journal of Biological Macromolecules, 2015. **80**: p. 121-129.
66. Watermann, B.T., et al., *Bioassays and selected chemical analysis of biocide-free antifouling coatings*. Chemosphere, 2005. **60**(11): p. 1530-1541.
67. Li, L.-H., et al., *Synthesis and characterization of chitosan/ZnO nanoparticle composite membranes*. Carbohydrate Research, 2010. **345**(8): p. 994-998.
68. Reddy, K.M., et al., *Selective toxicity of zinc oxide nanoparticles to prokaryotic and eukaryotic systems*. Applied Physics Letters, 2007. **90**(21): p. 213902.
69. Emamifar, A., et al., *Evaluation of nanocomposite packaging containing Ag and ZnO on shelf life of fresh orange juice*. Innovative Food Science & Emerging Technologies, 2010. **11**(4): p. 742-748.
70. Yamamoto, O., *Influence of particle size on the antibacterial activity of zinc oxide*. International Journal of Inorganic Materials, 2001. **3**(7): p. 643-646.
71. Sawai, J., et al., *Hydrogen peroxide as an antibacterial factor in zinc oxide powder slurry*. Journal of Fermentation and Bioengineering, 1998. **86**(5): p. 521-522.
72. Abiraman, T., et al., *Antifouling behavior of chitosan adorned zinc oxide nanorods*. RSC Advances, 2016. **6**(73): p. 69206-69217.
73. Pasquet, J., et al., *The contribution of zinc ions to the antimicrobial activity of zinc oxide*. Colloids and Surfaces A: Physicochemical and Engineering Aspects, 2014. **457**: p. 263-274.
74. Ahlafi, H., et al., *Kinetics of N-Deacetylation of Chitin Extracted from Shrimp Shells Collected from Coastal Area of Morocco*. Mediterranean Journal of Chemistry, 2013. **2**: p. 503-513.
75. Kim, J., et al., *Improved suspension stability of calcium carbonate nanoparticles by surface modification with oleic acid and phospholipid*. Biotechnology and Bioprocess Engineering, 2015. **20**(4): p. 794-799.
76. *Crosslinking Technical Handbook*. Available from: <https://tools.thermofisher.com/content/sfs/brochures/1602163-Crosslinking-Reagents-Handbook.pdf>.
77. Kildeeva, N.R., et al., *About mechanism of chitosan cross-linking with glutaraldehyde*. Russian Journal of Bioorganic Chemistry, 2009. **35**(3): p. 360.
78. Monteiro, O.A.C. and C. Airoidi, *Some studies of crosslinking chitosan–glutaraldehyde interaction in a homogeneous system*. International Journal of Biological Macromolecules, 1999. **26**(2): p. 119-128.
79. Luk, C., et al., *A Comprehensive Study on Adsorption Behaviour of Direct, Reactive and Acid Dyes on Crosslinked and Non-crosslinked Chitosan Beads*. 2014.
80. Cecchet, F., et al., *Redox Mediation at 11-Mercaptoundecanoic Acid Self-Assembled Monolayers on Gold*. The Journal of Physical Chemistry B, 2006. **110**(5): p. 2241-2248.
81. Dadafarin, H., E. Konkov, and S. Omanovic, *Electrochemical Functionalization of a 316L Stainless Steel Surface with a 11-mercaptoundecanoic Acid Monolayer: Stability Studies*. International Journal of Electrochemical Science, 2013. **8**: p. 369-389.
82. Sun, S.T., et al., *Bio-Inspired *In Situ* Fabrication of 11-Mercaptoundecanoic Acid Coating on Stainless Steel 304 for Corrosion Protection*. Materials Science Forum, 2018. **913**: p. 375-383.
83. Garcia, R.B.R., F.S. Silva, and E.Y. Kawachi, *Evaluation of dip and spray coating techniques in corrosion inhibition of AA2024 alloy using a silicon/zirconium sol-gel film as coating*. 2017, Author(s).

84. Xu, G., et al., *Tannic acid anchored layer-by-layer covalent deposition of parasin I peptide for antifouling and antimicrobial coatings*. RSC Advances, 2016. **6**(18): p. 14809-14818.
85. An, X., Y. Kang, and G. Li, *The interaction between chitosan and tannic acid calculated based on the density functional theory*. Chemical Physics, 2019. **520**: p. 100-107.
86. Smith, R.A., et al., *Single-Step Self-Assembly and Physical Crosslinking of PEGylated Chitosan Nanoparticles by Tannic Acid*. Polymers, 2019. **11**(5): p. 749.
87. Muzzarelli, R.A.A. and R. Rocchetti, *Determination of the degree of acetylation of chitosans by first derivative ultraviolet spectrophotometry*. Carbohydrate Polymers, 1985. **5**(6): p. 461-472.
88. Czechowska-Biskup, R., et al., *Determination of degree of deacetylation of chitosan - Comparison of methods*. Progress on Chemistry and Application of Chitin and its Derivatives, 2012. **2012**: p. 5-20.
89. Serdechnova, M., et al., *Photodegradation of 2-mercaptobenzothiazole and 1,2,3-benzotriazole corrosion inhibitors in aqueous solutions and organic solvents*. Phys. Chem. Chem. Phys., 2014. **16**(45): p. 25152-25160.
90. 2015; Available from: https://www.rutcm.ms.mcam.ac.uk/images/eng_atoms_images/sem-schematic/image_view_fullscreen.
91. 2014; Available from: <http://chemists.princeton.edu/bernasek/files/2014/08/atr-ftir.png>.
92. Fayyad, E., et al., *Evaluation techniques for the corrosion resistance of self-healing coatings*. 2014.
93. Yabuki, A. and K. Okumura, *Self-healing coatings using superabsorbent polymers for corrosion inhibition in carbon steel*. Corrosion Science, 2012. **59**: p. 258-262.
94. Weinhold, M.X., et al., *Strategy to improve the characterization of chitosan for sustainable biomedical applications: SAR guided multi-dimensional analysis*. Green Chemistry, 2009. **11**(4): p. 498.
95. Fernandes Queiroz, M., et al., *Does the use of chitosan contribute to oxalate kidney stone formation?* Marine drugs, 2014. **13**(1): p. 141-158.

TRITA ITM-EX 2020:435